From Rheic to Paleotethys: Subduction history of the Shanderman Eclogites (NW Iran)

Daniel Pastor-Galán[1,2], Alicia López-Carmona[3,†], Mahnaz Rezaeian[4], Tatsuki Tsujimori[5], Gabriel Gutiérrez-Alonso[6], Keewook Yi[7], and Cor Langereis[8]

[1]*Instituto de Geociencias, Consejo Superior de Investigaciones Científicas, Universidad Complutense de Madrid, Madrid 28040, Spain*
[2]*Frontier Research Institute for Interdisciplinary Science, Tohoku University, Sendai 980-8578, Japan*
[3]*Departamento de Mineralogía y Petrología, Universidad Complutense de Madrid, Madrid 28040, Spain*
[4]*Department of Earth Sciences, Institute for Advanced Studies in the Basic Sciences, Zanjan 45137-66731, Iran*
[5]*Department Earth Science, Graduate School of Science, Tohoku University, Sendai 980-8578, Japan*
[6]*Departamento de Geología, Universidad de Salamanca, Salamanca 37008, Spain*
[7]*Korea Basic Science Institute, Ochang 28119, Republic of Korea*
[8]*Paleomagnetic Laboratory Fort Hoofddijk, Utrecht University, 3584 CD Utrecht, Netherlands*

ABSTRACT

Pre-Jurassic plate reconstructions rely mainly on ophiolites and metabasites found along suture zones and plate boundaries. Tethyan oceanic rocks have undergone at least four Wilson cycles, characterized by Gondwana-derived continental terranes detaching and later accreting onto Laurussia/Eurasia, offering an excellent case example to understand long-term tectonic processes. The oceanic rocks from present-day north Turkey to northeast Iran contain an excellent record of those cycles. In this paper, we focus on the origins and tectonometamorphic evolution of the Shanderman eclogites in NW Iran. We have performed thorough petrological, Sm-Nd isochron, and U-Pb/Lu-Hf on zircon analyses. Our results show that the Shanderman eclogites' protoliths, basalts with mid-ocean ridge signature, underwent a maximum pressure of 2.25 GPa (~80 km) at ca. 350 Ma based on a Sm-Nd isochron in garnet. In one of the studied samples, we found a series of inherited zircon grains with Precambrian age that suggests the basaltic rocks formed or evolved in proximity to a Gondwana-derived terrane. In addition, we found a population of Paleozoic zircon grains, including a single zircon with a U-Pb age of ca. 350 Ma, possibly indicating that the oceanic crust formed immediately before subduction and metamorphism. The population of zircon with ages of ca. 280 Ma is compatible with a hydrothermal origin. We interpret that the Shanderman eclogites represent a piece of the Rheic (aka, Ran or Prototethys) that formed in the Carboniferous while the Pontide-Kopeh Dagh terrane migrated northward during the opening of the Paleotethys. The final consumption of the Rheic ocean produced the collision between the Pontide-Kopeh Dagh terrane during the late Carboniferous. Finally in the Early Permian the Paleotethys began subducting beneath Eurasia.

1. INTRODUCTION

Plate tectonic models are essential for unraveling Earth's history, helping us decipher everything from global geodynamics to the evolution of climate and ecosystems, while also aiding in the discovery of natural resources. Yet, because all oceanic lithosphere older than 200 m.y. has subducted and been recycled into the mantle and tomographic images provide only a limited snapshot of subduction history (only to ca. 290 Ma), our plate reconstructions become increasingly fragmented as we look farther back in time (e.g., Domeier and Torsvik, 2019). For any pre-Jurassic plate reconstruction, the only direct source of information about the processes and kinematics of the oceanic lithosphere are preserved in ophiolitic rocks and metabasites along suture zones and plate boundaries (e.g., Dewey and Burke, 1973; Moores, 1981; Platt, 1986; Liou et al., 1989; Tsujimori et al., 2006; López-Carmona et al., 2014; Tsujimori and Ernst, 2014; Ganbat et al., 2021). Eclogites are metamorphosed mafic rocks, typically consisting of garnet and omphacite, sometimes accompanied by minerals like kyanite, rutile, quartz/coesite, and others. Eclogite-facies rocks typically represent high-pressure (HP) to ultrahigh-pressure (UHP) metamorphic conditions, characterized by a relatively low geothermal gradient and the deep subduction of crust (e.g., Coleman et al., 1965; Tsujimori and Mattinson, 2021; Halama, 2024). Our only way to reconstruct oceanic plates in pre-Mesozoic tectonic models is through the oceanic relics emplaced over the continents.

During the Paleozoic era most continental plates of the Earth collided and merged, eventually forming the rigid superplate known as Pangea (Wegener 1912; Dietz and Holden, 1970; Stampfli et al., 2013; Domeier and Torsvik, 2014; Pastor-Galán, 2022). The resulting orogens involved the closure of major oceans and seaways (e.g., Van der Voo and French, 1974; Nance et al., 2010; Pastor-Galán et al., 2019). Today, the only remnants of these oceans and seaways are high-pressure–low-temperature (HP-LT) metamorphic rocks that are found along the sutures between continents (Nance et al., 2010). While northwestern Europe and eastern North America remained relatively stable during the existence of Pangea, the Tethyan realm stretching from southwestern Europe to southeast Asia experienced a prolonged history of tectonic activity, including subduction, collisions, and break-ups (Şengör, 1979; Jenkyns, 1980; Van der Voo, 1993; van Hinsbergen et al., 2020).

The Tethyan realm sensu lato, stretching over 15,000 km, offers a unique perspective on Earth's tectonic evolution, having experienced arguably four complete Wilson Cycles: Iapetus,

Alicia López-Carmona [ORCID] https://orcid.org/0000-0002-2513-6559
[†]acarmona@ucm.es

Rheic, Paleotethys, and Neotethys (e.g., Van der Voo, 1993; Nance et al., 2010; Domeier, 2016; van Hinsbergen et al., 2020). These cycles, which involve the repeated detachment of Gondwana-derived continents and their subsequent accretion onto Laurussia/Eurasia, have driven the progressive fragmentation of Gondwana throughout the Phanerozoic (e.g., du Toit, 1937; Şengör, 1990; Wu et al., 2021). Whereas the seafloor history of most of the Neotethyan and late Paleotethyan is preserved or observable through tomography (e.g., van Hinsbergen et al., 2020), the early Paleotethyan history and the Rheic or Iapetus requires relics of the oceanic lithosphere preserved over the continents (e.g., Mackay-Champion et al., 2024).

The Pontide-Caucasus-Talesh-Alborz-Kopeh Dagh system (present-day north Turkey to northeast Iran; Fig. 1) contains an excellent record of the amalgamation and break-up of Pangea's internal ocean realms (Berberian and King, 1981; Şengör et al., 1984; Şengör, 1990). The basement of the system corresponds with volcano-sedimentary sequences that commenced at ca. 700 Ma and lasted until ca. 460 Ma in general and until 400 Ma in the Transcaucasian area known as "Cadomian," interpreted as a long-lasting continental arc of northern Gondwana and the subsequent volcanism associated with its rift-to-drift transition (e.g., Berberian and King, 1981; Linnemann et al., 2008; Nance et al., 2010; Rolland et al., 2016; Rolland, 2017; Akdoğan et al., 2021). To the south of the Pontide-Kopeh Dagh system, at present we find the relics of the Cimmerian ribbon continent (e.g., Şengör et al., 1984; Jamei et al., 2021), another Gondwana derived group of crustal blocks, whose relics span today from Turkey to Malaysia (e.g., Şengör et al., 1984) or NW Iran to Malaysia (e.g., Topuz et al., 2013). In this paper we evaluate the subduction history of the Tethyan-type oceans with new petrologic and geochronology from the Shanderman metamorphic complex in NW Iran. Combined with available regional data and local data, we investigate the possible origins of the eclogitic protolith as well as its subducting history to improve our understanding of the geodynamics of the Tethyan oceans sensu lato.

2. GEOLOGICAL SETTING

The Paleozoic and Mesozoic tectonic evolution of the Pontide-Kopeh Dagh system (Fig. 1A) was dominated by the opening and closure of at least three major oceans (Rheic, Paleotethys, and Neotethys), along with several minor oceanic basins that separated Laurussia/Laurasia, Gondwana, and several arcs and microcontinents (e.g., Stampfli et al., 2013; Domeier

and Torsvik, 2014; Rolland et al., 2016; Vasey et al., 2020; Akdoğan et al., 2021). The opening of these major oceans was accompanied by the detachment and northward migration of ribbon continents and/or groups of continental blocks of various sizes from Gondwana to Laurussia/Laurasia (e.g., McKenzie, 1972; Rotstein and Kafka, 1982; Rolland et al., 2016; van Hinsbergen et al., 2020, and references therein). During the Neoproterozoic and earliest Cambrian, before the opening of the Rheic ocean (also known as Prototethys or Ran, especially on its east side; Domeier, 2016), the African-Arabian margin of Gondwana was characterized by a long active margin that developed the Cadomian arc (e.g., Berberian and King, 1981; Murphy and Nance, 1989; Sánchez-García et al., 2014, 2019; Nance et al., 2010, and references therein). Today, the remnants of the Cadomian arc stretch from Iberia across central and southeast Europe, Turkey, Iran, and Tibet-Tarim (e.g., Pereira et al., 2011; Moghadam et al., 2017).

The Rheic ocean opened diachronically from ca. 490 Ma in its western side to ca. 460 Ma in its eastern end (e.g., Stampfli et al., 2013). The opening mechanism of the Rheic ocean is disputed: it may have originated as a back-arc basin, a slab-pull effect after the subduction of a ridge (e.g., Murphy et al., 2006), or a combination of both (e.g., Nance et al., 2010). Along with the opening of the Rheic ocean, one or several continental fragments drifted from Gondwana to collide during the Silurian with Laurentia, Baltica (Nance et al., 2010), and perhaps other terranes in the Central Asian Orogenic belt (e.g., Stampfli et al., 2013).

During the Early Devonian, subduction zones were already consuming the Rheic-Ran ocean (e.g., Nance et al., 2010, and references therein), and by Middle Devonian times, the Rheic-Ran realm of Gondwana was recording an extensional event that some interpreted as the opening of the Paleotethys ocean (e.g., Gutiérrez-Alonso et al., 2008a; Stampfli et al., 2013; Guan et al., 2021). The Pontides-Transcaucasus belt probably migrated as a ribbon continent that rifted away from Gondwana during that time (e.g., Rolland et al., 2016; Akdoğan et al., 2021). During the Late Devonian and Early Mississippian, the Rheic ocean and its subsidiary basins that existed between Laurussia and Gondwana closed (e.g., Domeier and Torsvik, 2014; Wu et al., 2021), ending in the continent-continent collision that formed Pangea to the west (e.g., Stampfli et al., 2013; Weil et al., 2013). Based on the occurrence of igneous and high-temperature rocks, Rolland et al. (2016) suggested a polarity of subduction of the Rheic to the south in the Pontide-Kopeh Dagh system (i.e., the Pontide-Kopeh Dagh being the upper plate).

There is a long-standing debate on the mechanisms that triggered the opening of the Paleotethys, the number of continental fragments that drifted, and the quantity and type of oceanic basins that opened (cf. Nance et al., 2010; Stampfli et al., 2013; Domeier and Torsvik, 2014; Wu et al., 2021). The opening of the western Paleotethys was interrupted soon after its inception at its western margin due to the final amalgamation of Pangea (e.g., Pastor-Galán, 2022). However, the eastern Paleotethys side continued to grow during most of the late Paleozoic. Some researchers think that subduction in the Paleotethys was operating from the early stages of its opening (e.g., Stampfli et al., 2013), while others suggest that subduction initiated after the collision of the peri-Gondwana drifted terranes against the Eurasian margin of the ocean (e.g., Rolland et al., 2016; Vasey et al., 2020; Akdoğan et al., 2021).

During the latest stages of the amalgamation of Pangea (e.g., Gutiérrez-Alonso et al., 2008b; Pastor-Galán, 2022), and likely assisted by plume volcanism (e.g., Shellnutt et al., 2011; Torsvik and Cocks, 2013; Jamei et al., 2021), the Paleotethyan margin of Gondwana began to rift until the Neotethys ocean opened with the formation of the Cimmerian plate (e.g., Şengör et al., 1988). The Neotethys grew as Cimmeria migrated northward during the Permian and finally collided with Laurasia (the Turan platform) in the Triassic. Subduction initiated at various moments in the Neotethys during Jurassic and Cretaceous times, consuming most of it during the Cenozoic and forming the Alpine-Himalayan system (see van Hinsbergen et al., 2020, for a review of the Mesozoic and Cenozoic evolution of the Tethyan realm). The remnants of the three oceans can be found from Iberia to eastern Asia (e.g., Kirby 1979; Berberian and King, 1981).

2.1. Three Oceans' History

The three oceans' history is recorded by several suture zones that become younger southward within the Pontide-Kopeh-Dagh orogenic system (e.g., Rolland et al., 2016). In Iran, the northernmost ocean-derived rocks with different Paleozoic ages have been traditionally interpreted as remnants of the Paleotethys and the basins and/or seaways that separated the Gondwana derived Cimmerian microcontinents from the Eurasian margin (Central Iranian, Lut, Sanandaj-Sirjan, Alborz, and Kopeh Dagh, e.g., Şengör, 1984; Berberian and King, 1981; Zanchi et al., 2009a; Fig. 1B). The oceanic affinity rocks and ophiolites sensu stricto with Mesozoic ages, are typically interpreted as Neotethyan relics including the seaways and back-arcs that formed along previous sutures (e.g., Moghadam
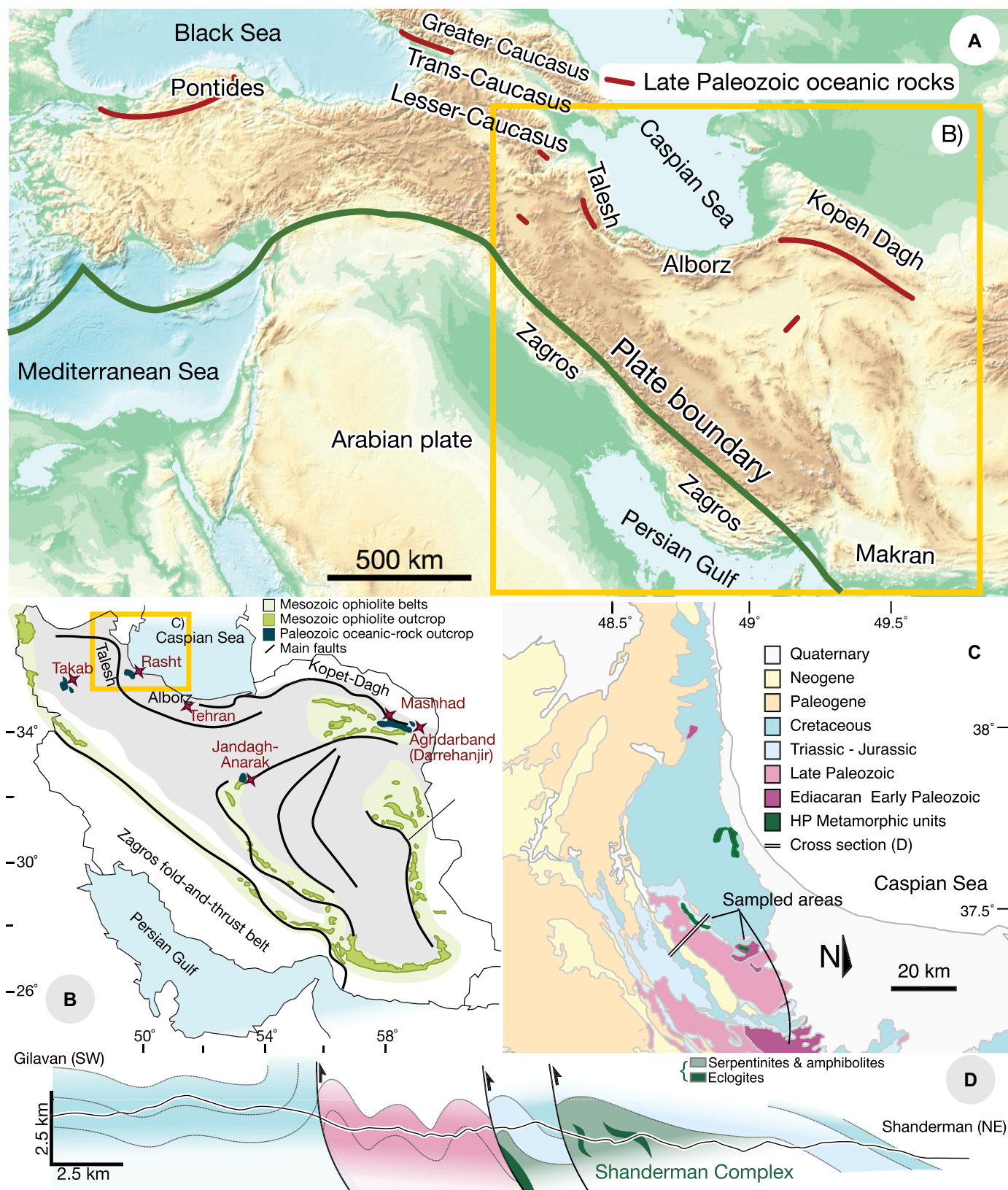
Figure 1. (A) Geographical location of the Pontide-Kopeh Dagh system and potential suture zones of Paleozoic oceans. (B) Location of the Mesozoic ophiolite and Paleozoic oceanic rocks that underwent high-pressure (HP) conditions. (C) Simplified geological map of NW Iran with the sampled areas after Clark et al. (1975). (D) Schematic cross-section between the localities of Gilan and Shanderman based on Clark et al. (1975).

Geological Society of America Bulletin

and Stern, 2015). Paleozoic oceanic rocks are found in two main regions in northern Iran: the first group closer to the northern boundaries of Iran (from east to west: Aghdarband, Mashad, Rasht, and Allahyarlu areas) and a second group JanDag-Anarak and Takab, to the south of them (Moghadam and Stern, 2014; Moazzen et al., 2020; Fig. 1B).

The Aghdarband-Mashhad oceanic complex is in the Kopeh Dagh (Fig. 1B) and includes a Permian ophiolite and pelagic sediments in fault contact with an outcrop of Devonian intrusive and ultramafic rocks (ca. 380 Ma, zircon U-Pb in tonalites) with mid-ocean ridge basalt (MORB), boninitic and calc-alkaline signatures (Darrehanjir; Moghadam and Stern, 2015). The ophiolites (in the Kopeh Dagh) consist of serpentinized peridotite, gabbro mafic volcanic rocks, and pelagic sedimentary rocks (carbonates, tuffs, radiolarites) with Early Permian ages, with a volcano-sedimentary complex developed over them (Moghadam and Stern, 2014, and references therein). Some of these ophiolites are intruded by Late Triassic granitoids (Karimpour et al., 2010, Mirnejad et al., 2013).

The Anarak, Jandaq, and Posht-e-Badam (Anarak complex hereafter) complexes are located within the NW sector of the central Iranian block (Fig. 1B). The Anarak complex contains dismembered ophiolites (in fault contact with the Late Cretaceous Nain-Ashin ophiolites; Fig. 1B) and deformed siliciclastic, calcareous, and volcanic rocks with various metamorphic grades. The Anarak complex includes a Late Ordovician to Carboniferous accretionary complex (so-called "Variscan accretionary complex") with a thick and fine grain siliciclastic sequence accompanied by marginal-sea oceanic remnants, including gabbro-basalts with a supra-subduction-geochemical signature. This complex underwent greenschist to amphibolite facies with $^{40}Ar/^{39}Ar$ muscovite plateau ages of ca. 333–320 Ma (Bagheri and Stampfli, 2008). In the Anarak complex, to the south of the "Variscan accretionary complex," there is a younger Permian–Triassic accretionary complex, which includes the relics of two seamounts (Anarak and Kabudan) and dismembered ocean floor members including peridotite intruded by gabbroic dikes, trondhjemite (plagiogranite), and pillow lavas (ocean island basalt type). U-Pb zircon dating of the trondhjemite is Permian (ca. 262 Ma), ~120 m.y. younger than the ocean floor found in the Aghdarband-Mashhad oceanic complex. The Permian–Triassic accretionary complex underwent blueschist facies (HP-LT) metamorphism during the Late Triassic (ca. 232 Ma $^{40}Ar/^{39}Ar$ plateau age in stilpnomelane, Bagheri and Stampfli, 2008), an age that coincides with the beginning of the Cimmerian Orogeny (e.g., Bagheri and Stampfli, 2008). The westernmost Allahyarlu complex comprises metapelites and metabasites that experienced amphibolite-facies metamorphism at ca. 326–334 Ma (Ar-Ar on muscovite; Moazzen et al., 2020). Geochemical evidence indicates that the metabasite protoliths formed in a continental back-arc setting. Moazzen et al. (2020) interpreted the Allahyarlu complex as the product of an active continental margin arc, marking the onset of continental collision.

2.2. The Talesh and Its High Pressure–Low Temperature Rock Record

The Talesh is a 200-km-long mountain chain with a "Z" shape in map view in NW Iran (Figs. 1B and 1C), wrapping the southwest margin of the Caspian Sea, defining a conspicuous N-S oriented segment within the predominantly E-W oriented Pontides-Lesser Caucasus-Talesh-

TABLE 1. REPRESENTATIVE MICROPROBE ANALYSES IN SAMPLE T20B, SHANDERMAN ECLOGITES, NW IRAN

Mineral	Garnet porphyroblasts (S₁)						Matrix (S₂)						Matrix (post-S₂)						
	Grt1$_C$	Grt1$_R$	Grt2$_C$	Grt2$_R$	Czo	Pg	Omp	Gln	Brs	Wnc	Czo	Pg	Pg	Act	Hbl	Ed	Ilm	Chl	Ab
SiO$_2$	37.70	37.57	37.71	38.07	39.22	46.14	56.14	57.60	50.80	54.38	38.88	46.64	47.47	54.58	49.19	47.62	0.01	25.05	68.25
TiO$_2$	0.12	0.16	0.07	0.08	0.10	0.00	0.08	0.06	0.06	0.08	0.12	0.02	0.07	0.03	0.12	0.00	55.85	0.16	0.00
Al$_2$O$_3$	22.18	21.87	22.55	22.94	30.48	40.48	9.39	12.39	9.39	7.56	30.45	39.67	39.60	8.54	10.87	12.41	0.00	20.38	20.18
Cr$_2$O$_3$	0.01	0.28	0.03	0.01	0.00	0.08	0.25	0.00	0.00	0.00	0.00	0.06	0.05	0.01	0.00	0.00	0.00	0.02	0.00
Fe$_2$O$_3$	0.00	0.22	0.00	2.01	4.78	0.00	3.46	0.51	0.62	0.53	4.35	0.00	0.00	0.00	0.73	0.00	0.00	0.00	0.23
FeO	19.43	24.73	27.33	20.81	0.44	0.64	3.85	5.74	8.62	7.45	0.25	0.12	0.33	6.14	8.36	11.78	40.44	29.22	0.00
MnO	12.02	3.40	2.25	0.10	0.19	0.00	0.36	0.00	0.10	0.02	0.10	0.00	0.03	0.03	0.03	0.01	5.60	0.50	0.00
MgO	0.87	1.55	1.46	7.54	0.04	0.03	7.49	12.44	14.65	15.63	0.07	0.14	0.45	15.83	14.97	11.94	0.05	11.41	0.00
CaO	9.15	10.84	8.76	8.75	24.75	0.87	13.11	1.91	9.73	8.43	24.74	0.24	0.39	10.42	10.76	10.42	0.12	0.07	0.28
Na$_2$O	0.03	0.05	0.03	0.01	0.03	7.05	7.08	6.62	3.18	3.49	0.00	6.86	6.56	2.98	3.00	3.25	0.05	0.01	11.66
K$_2$O	0.00	0.00	0.00	0.00	0.01	0.19	0.05	0.06	0.06	0.08	0.00	0.05	1.03	0.02	0.11	0.11	0.00	0.00	0.01
Total	100.5	100.6	100.2	100.3	100	95.48	101.2	97.32	97.21	97.65	98.96	94.37	95.98	98.58	98.14	97.56	102.1	86.81	100.6
Oxygens	12	12	12	12	12.5	11	6	23	23	23	12.5	11	11	23	23	23	3	14	8
Si	2.97	2.96	2.98	2.91	2.97	2.94	2.00	7.81	7.23	7.59	2.97	3.00	3.01	7.51	6.97	6.88	0.00	2.73	2.97
Ti	0.01	0.01	0.00	0.00	0.01	0.00	0.00	0.01	0.01	0.01	0.01	0.00	0.00	0.00	0.01	0.00	1.03	0.01	0.00
Al	2.06	2.03	2.10	2.06	2.72	3.05	0.39	1.98	1.58	1.24	2.74	3.01	2.96	1.39	1.82	2.11	0.00	2.62	1.03
Cr	0.00	0.02	0.00	0.00	0.00	0.00	0.01	0.00	0.00	0.00	0.00	0.00	0.00	0.00	0.00	0.00	0.00	0.00	0.00
Fe^{3+}	0.00	0.01	0.00	0.12	0.27	0.00	0.09	0.05	0.07	0.06	0.25	0.00	0.00	0.00	0.08	0.00	0.00	0.00	0.01
Fe^{2+}	1.28	1.63	1.81	1.33	0.03	0.03	0.11	0.65	1.03	0.87	0.02	0.01	0.02	0.71	0.99	1.42	0.83	2.67	0.00
Mn	0.80	0.23	0.15	0.01	0.01	0.00	0.01	0.00	0.01	0.00	0.00	0.00	0.00	0.00	0.00	0.00	0.12	0.05	0.00
Mg	0.10	0.18	0.17	0.86	0.01	0.00	0.40	2.51	3.11	3.25	0.01	0.01	0.04	3.25	3.16	2.57	0.00	1.86	0.00
Ca	0.77	0.92	0.74	0.72	2.01	0.06	0.50	0.28	1.48	1.26	2.03	0.02	0.03	1.54	1.63	1.61	0.00	0.01	0.01
Na	0.00	0.01	0.01	0.00	0.00	0.87	0.49	1.74	0.88	0.94	0.00	0.86	0.81	0.80	0.82	0.91	0.00	0.00	0.98
K	0.00	0.00	0.00	0.00	0.00	0.02	2.00	0.01	0.01	0.01	0.00	0.05	0.08	0.00	0.02	0.02	0.00	0.00	0.00
Sum	8	8	8	8	8	7	4	15	15	15	8	7	7	15	15	15	2	10	5
X$_{Fe}$	0.93	0.90	0.91	0.61			0.22	0.21	0.25	0.21				0.18	0.24	0.36			
Alm	43.30	55.18	62.92	45.69															
Prp	3.45	6.16	5.99	29.49															
Grs	26.12	30.85	25.84	23.64															
Sps	27.13	7.65	5.26	0.23															
X$_{Fe3+}$					0.27			0.03	0.08	0.06	0.25					0.09			
X$_{Na}$						0.98						0.94	0.91						
Jd							49												
Di							51												
Na$_B$								1.7	0.49	0.71				0.6	0.32	0.38			
Ab																			99
An																			1

Notes: C—core; R—rim; Grt—garnet; Czo—clinozoisite; Pg—paragonite; Omp—omphacite; Gln—glaucophane; Brs—barroisite; Wnc—winchite; Act—actinolite; Hbl—hornblende; Ed—edenite; Ilm—ilmenite; Chl—chlorite; Alm—almandine; Prp—pyrope; Grs—grossular; Sps—spessartine; Jd—jadeite; Di—diopside; Ab—albite; An—anorthite. XFe = Fe^{2+}/(Fe^{2+}+Mg); Alm = Fe/(Fe + Mg + Ca + Mn); Prp = Mg/(Fe + Mg + Ca + Mn); Grs = Ca/(Fe + Mg + Ca + Mn); Sps = Mn/(Fe + Mg + Ca + Mn); XFe^{3+}(Czo) = Fe^{3+}/(Fe^{3+}+Al−2); XFe^{3+}(Amp) = Fe^{3+}/(Fe^{3+}+AlVI); XNa(Pg) = Na/(Na + K); Jd = (Na− Fe^{3+})/(Fe^{3+}(Na-Fe^{3+})+Ca); Di = Ca/(Fe^{3+}(Na-Fe^{3+})+Ca); Ab = Na/(Na + Ca + K); An = Ca/(Na + Ca + K); NaB = amount of Na in B position

Alborz-Kopeh Dagh system (Fig. 1C; Rezaeian et al., 2020). The geological record of the Talesh spans from the Ediacaran to the present day. Together with the Zagros Mountains, the Talesh and Alborz mountains accommodated most of the shortening related to the Cenozoic Arabia-Eurasia convergence (Mattei et al., 2017; van der Boon et al., 2018). The present-day elevation of the Talesh mountains is the result of the development of a shallow fold-and-thrust belt and orocline bending that occurred during the Arabia-Eurasia collision (Madanipour et al., 2017; van der Boon et al., 2018; Rezaeian et al., 2020) and consumption of the Transcaucasus basin in the Eocene (Shiva et al., 2025).

The pre-Mesozoic geology of the Talesh Mountains consists of a non-metamorphic stratigraphic sequence comprising calcareous beds intercalated with mafic volcanic rocks and clastic sediments in the northern margin of the Iran block. This sequence exhibits North Gondwana (Arabia) affinity (Honarmand et al., 2018). Above a Triassic hiatus with a prominent angular unconformity marking the Cimmerian orogeny (e.g., Zanchi et al., 2009a, 2009b), the stratigraphic succession continues with up to 3400 m of Jurassic–Cretaceous clastic, calcareous, and volcanic rocks, followed by an over 9-km-thick Cenozoic continental arc volcano-sedimentary sequence (Rezaeian et al., 2020, and references therein). Tectonically embedded on the non-metamorphic Phanerozoic series is a series of metamorphic outcrops in the Talesh that we group under the name "Rasht complex." The Rasht complex includes the HP-LT rocks in Shanderman and Asalem (e.g., Omrani et al., 2013; Rossetti et al., 2017) and a medium-pressure–medium-temperature (MP-MT) larger complex, the Ghast outcrop (Fig. 1B). The Gasht outcrop contains two units with different metamorphic histories: a lower succession with medium-grade metapelite, amphibolite, and gneiss (sillimanite-, kyanite-, and staurolite-bearing) (Zanchetta et al., 2009, Zanchi et al., 2009a) and a low-grade upper unit (slate, phyllite, and quartzites). Phyllite near Masuleh yielded whole-rock Rb-Sr isochron ages of 382 ± 48 Ma and 375 ± 12 Ma (Crawford, 1977).

The Shanderman Complex crops out in a small erosional window below the Mesozoic units between the Rud-e-Masal and Asalem. The Shanderman HP-LT rocks comprise deformed slate, phyllite, gneiss, and amphibolite, along with patches of serpentinized peridotite and eclogites (Omrani et al., 2013). The geochemistry of metabasites in the Shanderman complex is normal (N)-MORB (Omrani et al., 2013; Wan et al., 2021). Although the contacts are poorly exposed, mafic intrusions and ultramafic cumulates (occasionally layered with rare felsic rocks)

are observed to intrude the eclogites (Zanchetta et al., 2009). The eclogitic rocks are retrogressed to amphibolite and greenschist (e.g., Omrani et al., 2013). The peak metamorphism of the eclogites is disputed: Zanchetta et al. (2009) calculated 600–700 °C and P > 1.5 GPa; Omrani et al. (2013) proposed a higher pressure (1.5–2.0 GPa) but lower T ($\sim$600 °C); more recently, Wan et al. (2021) have suggested pressures close to the UHP metamorphism ($\sim$2.7 GPa) and T of $\sim$590 °C. Wan et al. (2021) interpreted the coincident 350 Ma ^{40}Ar/^{39}Ar dating in phengite and rutile U-Pb isochron as the peak metamorphism timing. A previous late Carboniferous ^{40}Ar/^{39}Ar age of 315 ± 9 Ma on paragonite was reported, but most steps in each plateau are mutually discordant (Zanchetta et al., 2009).

The Asalem metamorphic complex crops closer to the city of Asalem (Gilan Province, Iran) in an erosional window and below Mesozoic flat-lying sedimentary cover rocks (Rossetti et al., 2017). The Asalem complex consists of a mélange made of tectonic slices of metabasite and metapelites in greenschist and blueschist facies and serpentinized ultramafic rocks. The whole-rock geochemistry of the metabasites of Asalem shows MORB to arc signatures and has been interpreted as the remnants of a suprasubduction-type ophiolite generated at an active plate margin (Rossetti et al., 2017). Rossetti et al. (2017) interpreted a pressure-temperature (*P-T*) peak for the metapelites (chloritoid-garnet bearing schist) of 2.1 GPa and 470–510 °C (eclogite facies), whereas for the Na-rich amphibole metabasites reached 400 °C and 1 GPa (blueschist facies). The reconstructed *P-T* paths suggest isothermal decompression. ^{40}Ar/^{39}Ar in phengite exhibit plateau ages of 345–352 Ma, but metabasite samples also show younger ages (between 250 Ma and 290 Ma) in the LT part of the spectra, which imply partial Permian resetting.

Alavi (1991, 1996) and Şengör (1990) considered the oceanic relics of the Rasht area to be equivalent to the Aghdarband-Mashhad ophiolites both marking the Paleotethyan suture sensu lato. However, although the existing constraints might indicate that the protolith formed at a similar time (Moghadam and Stern, 2014), the Rasht complex was subducted to eclogitic conditions during the Carboniferous, likely in the Early Carboniferous (Zanchetta et al., 2009; Rossetti et al., 2017; Wan et al., 2021). Zanchetta et al. (2009) considered that the Shanderman complex does not mark the Paleotethys suture and instead represents an allochthonous nappe of Variscan continental crust, coming from the southern margin of the Transcaucasian region and stacked upon the northern margin of the Central Iranian block.

3. METHODS AND RESULTS

Rock samples were collected in the Rasht complex (Fig. 1B) in the HP-LT outcrop of Shanderman and MT-MP of Ghast. Samples for petrological analyses were drilled with an oil-powered drill, with cores of 2.5 cm diameter to obtain fresh samples.

3.1. Petrography, Mineral Chemistry, and Petrological Modeling

Mineral analyses and elemental X-ray maps were performed with a JEOL-Superprobe JXA-8900 M microprobe equipped with five spectrometers at the Unique Scientific and Technical Infrastructure National Center for Electron Microscopy at the Complutense University of Madrid (Madrid, Spain). The operating parameters for punctual analyses were: 15 kV accelerating voltage, 20 nA beam current, 5 μm beam diameter (1 μm for the microinclusions) and 10 s counting time on peak for each element. X-ray maps were operated at 20 kV and 150 nA. Representative analyses of selected minerals are listed in Table 1. Mineral formulae have been calculated using the software AX62 (https://filedn.com/lU1GlyFhv3UuXg5E9dbn-WFF/TJBHpages/index.html), which executes standard mineral recalculations, with attempts at ferric iron estimation from stoichiometric constraints. Mineral abbreviations are those proposed by Warr (2021): Ab—albite; Act—actinolite; Alm—almandine; An—anorthite; Brs—barroisite; Bt—biotite; Chl—chlorite; Coe—coesite; Czo—clinozoisite; Di—diopside; Ed—edenite; Grs—grossular; Grt—garnet; Gln—glaucophane; Hbl—hornblende; Hem—hematite; Ilm—ilmenite; Jd—jadeite; Ky—kyanite; Lws—lawsonite; Mag—magnetite; Ms—muscovite; Omp—omphacite; Pg—paragonite; Pl—plagioclase; Prp—pyrope; Qz—quartz; Rt—rutile; Sps—spessartine; Ttn—titanite; and Wnc—winchite. Other abbreviations: Cpx—clinopyroxene; Amp—amphibole; Carb—car-

TABLE 2. BULK-ROCK COMPOSITION FROM XRF ANALYSES OF SAMPLE T20B, SHANDERMAN ECLOGITES, NW IRAN, EXPRESSED IN WT% AND NORMALIZED IN MOL% TO THE NCKFMASHTO MODEL SYSTEM

Oxides	wt%	mol%
SiO_2	50.85	55.76
TiO_2	0.91	0.75
Al_2O_3	15.97	20.65
FeO	7.20	6.60
MnO	0.11	0.10
MgO	6.22	10.17
CaO	9.02	10.54
Na_2O	4.23	8.99
K_2O	0.30	0.42
P_2O_5	0.04	0.04
Fe_2O_3	1.66	1.37

Notes: XRF—X-ray fluorescence.
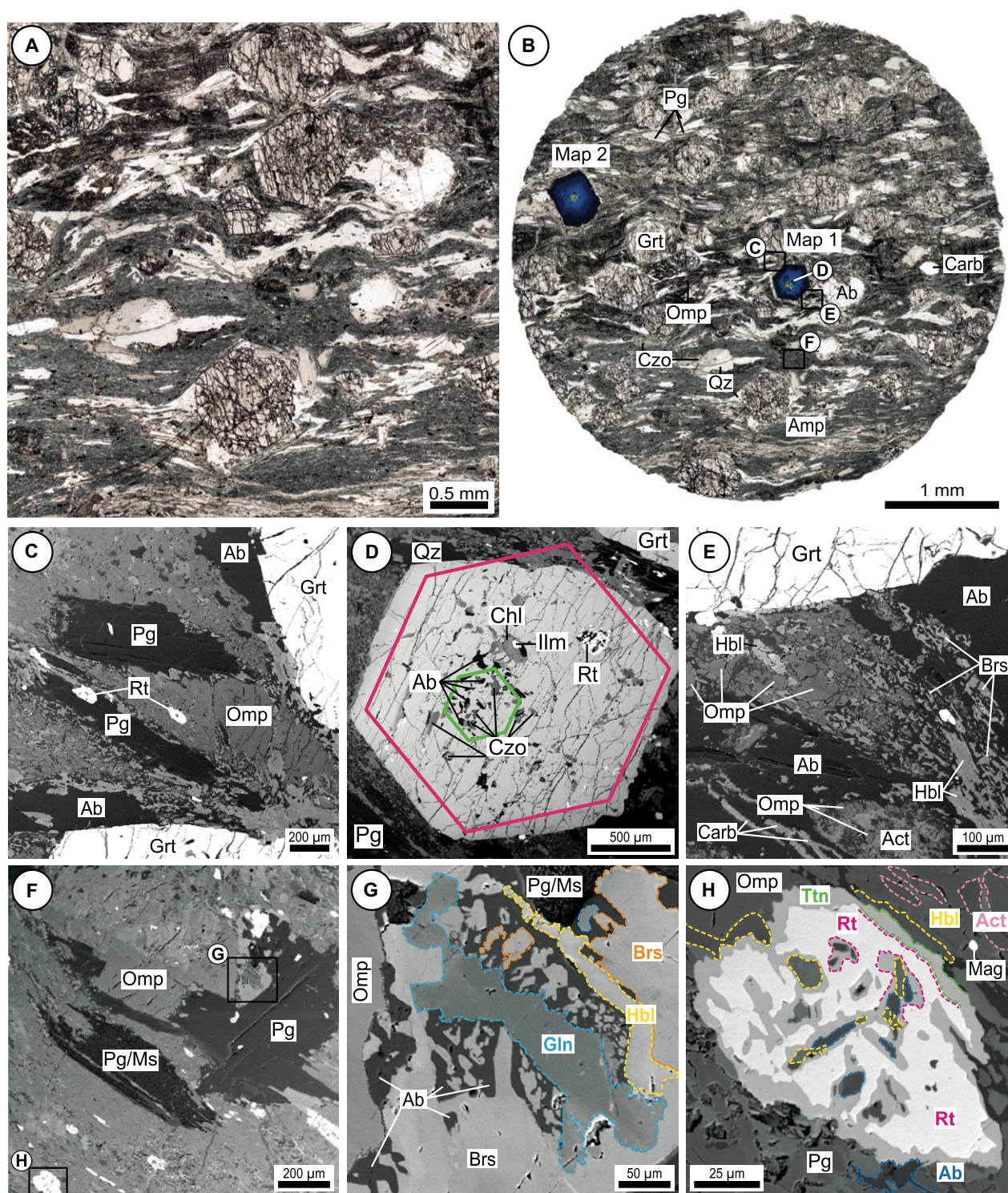
Figure 2. Microphotographs of thin-section images of Shanderman eclogites from NW Iran showing (A) the porphyronema-toblastic microtexture defined by omphacite (Omp) + clinozoisite (Czo) + glaucophane (Gln)/barriosite (Brs) + paragonite (Pg)/muscovite (Ms) + rutile (Rt) ± quartz (Qz) wrapping around garnet (Grt); (B) overall thin-section map showing the location of X-ray maps in garnets (Fig. 3) and different textural details. Back-scattered electron images showing detailed textures; (C) overview of matrix foliation (S₂); (D) inclusions in garnet porphyroblasts (S₁); (E) symplectitic intergrowth between Omp-Na and Ca-amphibole (Amp)-albite (Ab) and (F) Pg/Ms intergrowth in the S₂-foliation; (G) detail of the symplectites; and (H) titanite (Ttn) coronae around Rt. Act—actinolite; Chl—chlorite; Hbl—hornblende; Ilm—ilmenite. Mineral abbreviations are those proposed by Warr (2021).
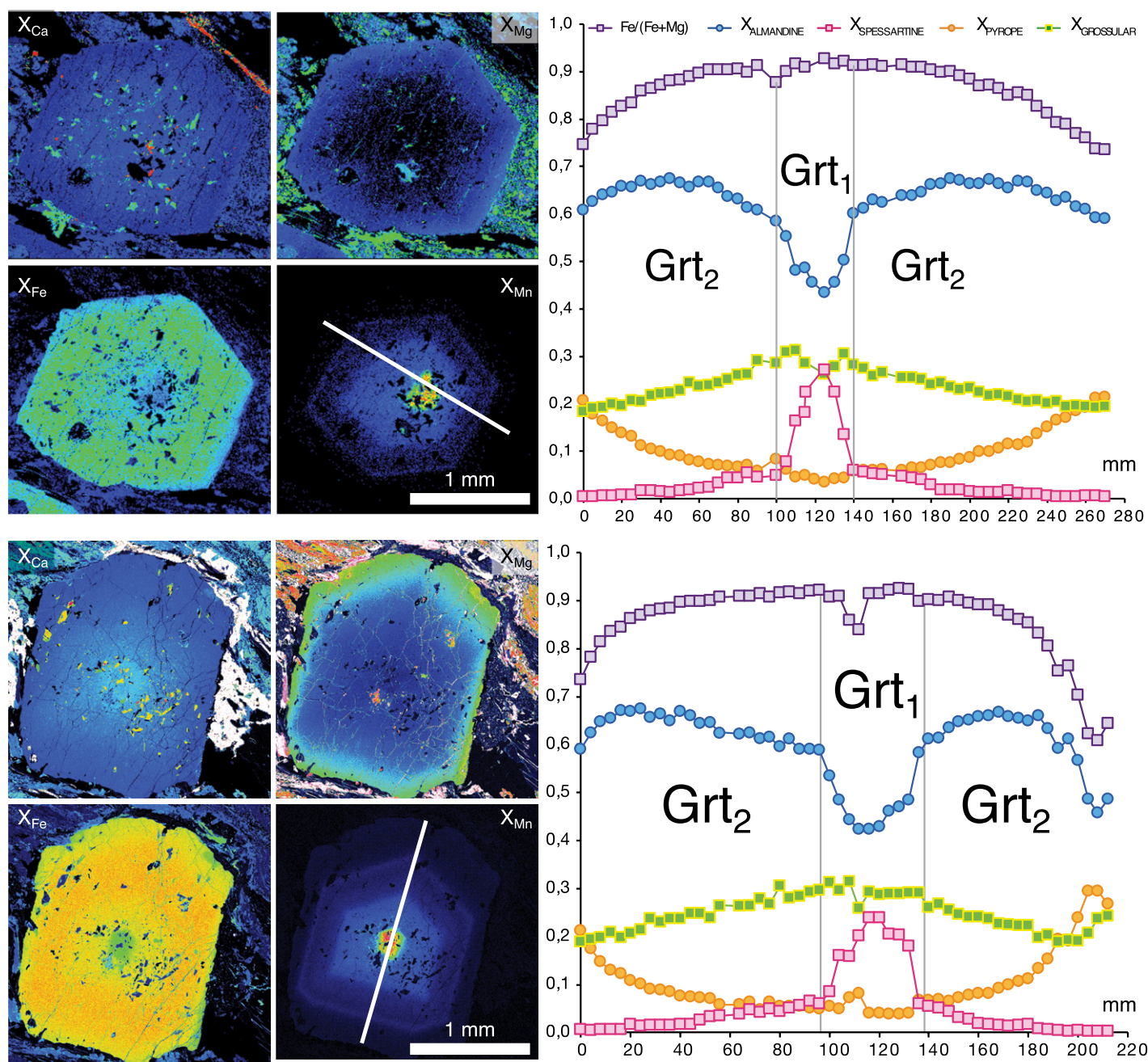
Figure 3. X-ray maps and chemical profiles illustrating zoning of euhedral garnet (Grt) porphyroblasts of Shanderman eclogites from NW Iran displaying an optical zoning interpreted as type 1 and 2 garnets. Thick lines on the X-ray maps indicate the position of the profiles.

bonate. Compositional variables: Alm = Fe/(Fe + Mg + Ca + Mn); Prp = Mg/(Fe + Mg + Ca + Mn); Grs = Ca/(Fe + Mg + Ca + Mn); Sps = Mn/(Fe + Mg + Ca + Mn); X_{Fe} = Fe^{2+}/(Fe^{2+}+Mg); X_{Fe3+}(Czo) = Fe^{3+}/(Fe^{3+}+Al−2); X_{Fe3+}(Amp) = Fe^{3+}/(Fe^{3+}+Al^{VI}); X_{Na}(Pg) = Na/(Na + K); Jd = (Na-Fe^{3+})/[Fe^{3+}(Na-Fe^{3+}) +Ca]; Di = Ca/[Fe^{3+}(Na-Fe^{3+}0] + Ca); Ab = Na/(Na + Ca + K); An = Ca/(Na + Ca + K).

P-T-composition (*P-T*-X) equilibrium phase diagrams (i.e., pseudosections) were calculated using Theriak-Domino software package (de Capitani and Brown, 1987; de Capitani and Petrakakis, 2010) in the model chemical system NCKFMASHTO (Na$_2$O-CaO-K$_2$O-FeO-MgO-Al$_2$O$_3$-SiO$_2$-H$_2$O-TiO$_2$-Fe$_2$O$_3$) using the internally consistent thermodynamic data set ds6.2 (Holland and Powell, 2011) converted to Theriak-Domino format by D.K. Tinkham (2016, personal commun.). References for the mixing models for solid solutions of the phases considered in the calculations are ilmenite-hematite (White et al., 2000); plagioclase (Holland and Powell, 2003); epidote (Holland and Powell, 2011); biotite, chlorite, garnet, and white mica (White et al., 2014); and amphibole and clinopyroxene (Holland and Blundy, 1994; Green et al., 2016). Albite, kyanite, lawsonite, magnetite, quartz, rutile, and titanite are considered as pure end members. Fluid was fixed as pure H$_2$O. There is a modal percentage (=∼5%) of calcium carbonate in the sample, but CO$_2$ has not been considered in the modeling. Textural
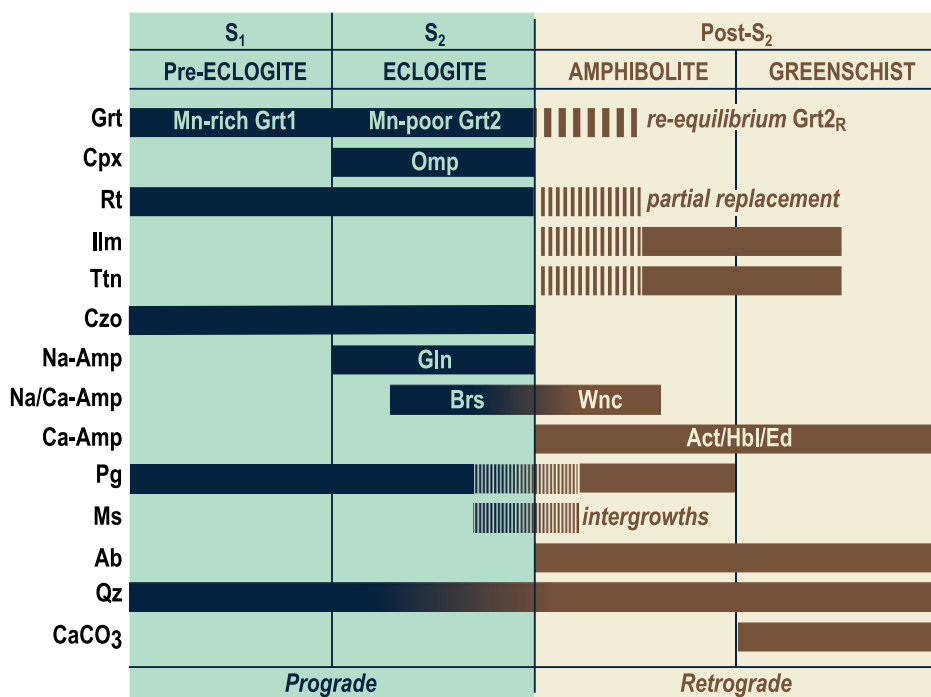
Figure 4. Diagram showing the blastesis-deformation relations in the Shanderman eclogites of NW Iran. Grt2$_R$—garnet 2 rim; Grt—garnet; Cpx—clinopyroxene; Rt—rutile; Ilm—ilmenite; Ttn—titanite; Czo—clinozoisite; Amp—amphibole; Pg—paragonite; Ms—muscovite; Ab—albite; Qz—quartz; Omp—omphacite; Gln—glaucophane; Brs—barroisite; Wnc—winchite; Act—actinolite; Hbl—hornblende; Ed—edenite. Mineral abbreviations are those proposed by Warr (2021).

observations suggest that the intervention of this fluid phase took place in the last stages of the *P-T* evolution of the rock. Bulk-rock composition was obtained at Activation Laboratories Ltd., Ancaster, Ontario, Canada, by X-ray fluorescence on a crushed rock slab of the most representative sample of the eclogite's lens from the Shanderman Complex (referred to hereafter as sample T20B). FeO (vs. Fe_2O_3) was analyzed by wet chemical titration and the amount of Fe_2O_3 is then calculated stoichiometrically as: [total iron/1.43 – (FeO/1.286) × 1.43]. The results have been converted to molar proportions and the amount of CaO was corrected for the presence of apatite (CaO$_{effective}$ = CaO$_{measured}$ – 3.33 × P_2O_5; see Table 2). Several *P-T*-X phase diagrams have been calculated to model the possible variations of different key components. MnO was not included in the chemical model system. Sample T20B has a low MnO content (0.11 wt%; Table 2), which is exclusively concentrated in garnet cores, in ilmenite replacing rutile, and in retrograde chlorite. Besides, the addition of MnO greatly influences the stability of garnet toward low-pressure fields and the resulting diagrams are topologically very similar to those calculated without MnO (White et al., 2014). Regardless of the nature of

the chemical system in which the mineral associations were equilibrated, neither CO_2, Na_2O, nor CaO undergo significant variations affecting the equilibrium of the eclogitic paragenesis. Nevertheless, H_2O strongly influences the solvus topology between sodium and calcium amphiboles. The preliminary model was calculated considering the fluid as pure H_2O, initially in excess, and the solvus is not represented at high pressures. Instead, kyanite-bearing fields increase their stability toward low pressures and clinozoisite is not stable in eclogitic paragenesis in the presence of garnet. By means of a *P*-X(H_2O) pseudosection calculated at 600 °C (maximum temperature at which the eclogitic assemblage is stable), a 25 mol% of H_2O has been estimated as the proportion necessary to reproduce the textural observations. Therefore, the whole-rock composition analyzed, inferring 25 mol% of free-H_2O in the rock, has been considered as the effective domain representative of the local equilibrium.

Sample T20B is an intensely foliated retro-eclogite (Fig. 2) with an Al-rich N-MORB chemical composition (Table 2; Omrani et al., 2013; Wan et al., 2021). The matrix shows a symplectitic texture in which almandine-rich garnet porphyroblasts dominate (=∼60%

modal). Precinematic garnet blasts are mostly euhedral (1–4 mm in diameter; Figs. 2A and 2B), highly fractured and show prograde zoning patterns. Garnet cores (almandine [Alm]$_{42\Rightarrow60}$pyrope [Prp]$_{0.3\Rightarrow0.8}$grossular [Grs]$_{26\Rightarrow31}$spessartine [Sps]$_{27\Rightarrow0.8}$, where "⇨"denotes core-to-rim variation; Fig. 3; Table 1), referred to as garnet 1 (Grt1), contain randomly oriented microinclusions (5–10 μm) of clinozoisite (X_{Fe3+} = 0.25–0.27; Mn < 0.01 per formula unit [pfu]), paragonite (X_{Na} = 0.98–1), rutile and secondary accessory Fe- and Mg-hornblende, chlorite, ilmenite, titanite, albite (Ab$_{0.93}$), calcium carbonate, and quartz filling fractures and voids (Fig. 2D). Toward the rim (Alm$_{61\Rightarrow67}$Prp$_{10\Rightarrow15}$Grs$_{27\Rightarrow19}$Sps$_{0.6\Rightarrow0}$; Fig. 3); in the outer part of the porphyroblasts (referred here to as garnet 2 [Grt2]), the same inclusions define a subtle internal foliation (S$_1$) that has unoriented or linear patterns and is oblique to the matrix foliation (S$_2$; Fig. 3). In the outermost rim (Grt2$_R$), almandine, grossular, and X_{Fe} first decrease before increasing again (Alm$_{67\Rightarrow46\Rightarrow49}$, Grs$_{27\Rightarrow19\Rightarrow24}$, X_{Fe} = 0.85⇨0.61⇨0.64), pyrope first increases (Prp$_{15\Rightarrow29}$) and then locally decreases (Prp$_{29\Rightarrow27}$). The matrix foliation, S$_2$, is defined by the shape preferred orientation of omphacite (>0.3 mm; jadeite$_{47–54}$; X_{Mg} > 0.76; Al pfu 0.39–0.54), glaucophane [>0.1 mm; Al^{VI} = 1.8; X_{Fe} = 0.21; X_{Fe3+} = 0.03; (Na + K)$_A$ = 0.05; Na$_B$ = 1.7], clinozoisite (>0.2 mm; X_{Fe3+} = 0.2–0.25; Mn < 0.01 pfu), paragonite (>0.3 mm; X_{Na} > 0.91), rutile (<60 μm), and accessory quartz (Figs. 2C–2E). Glaucophane is rimed by barroisite [>0.2 mm; X_{Mg} = 0.56–0.75; X_{Fe3+} = 0.05–0.14; (Na + K)$_A$ = 0.19–0.47; Na$_B$ = 0.5–0.75] showing bluish cores and pale-green rims (Fig. 2G). While barroisite is limited to the rim of sodic amphibole, winchite [>0.3 mm; X_{Mg} = 0.79; X_{Fe3+} = 0.06; (Na + K)$_A$ = 0.25; Na$_B$ = 0.71] occurs as allotrioblastic crystals, together with edenite [>0.2 mm; X_{Mg} = 0.64; (Na + K)$_A$ = 0.55; Na$_B$ = 0.38], in calcium carbonate-rich domains. S$_2$ foliation wraps gently around garnets. Post-S$_2$ foliation comprise partial or complete replacement of rutile, either by titanite or ilmenite (up to 6 wt% of MnO) (Fig. 2H), paragonite-muscovite intergrowths (<3 μm; below electron microprobe resolution), large post-kinematic paragonite crystals (up to 0.5 mm; oblique to S2), a pervasive calcium carbonate development and fine-grained symplectites (<20 μm) between omphacite-barroisite/glaucophane-albite (Ab = 93%–99%). Symplectites around glaucophane include the development of actinolite flakes [<10 μm; X_{Mg} = 0.82–0.84; (Na + K)$_A$ = 0.15–0.2; Na$_B$ = 0.4–0.6] blended by Mg-hornblende rims [<20 μm; X_{Mg} = 0.54–0.76; (Na + K)$_A$ = 0.48–0.52; Na$_B$ = 0.32–0.4; Figs. 2E and 2G].
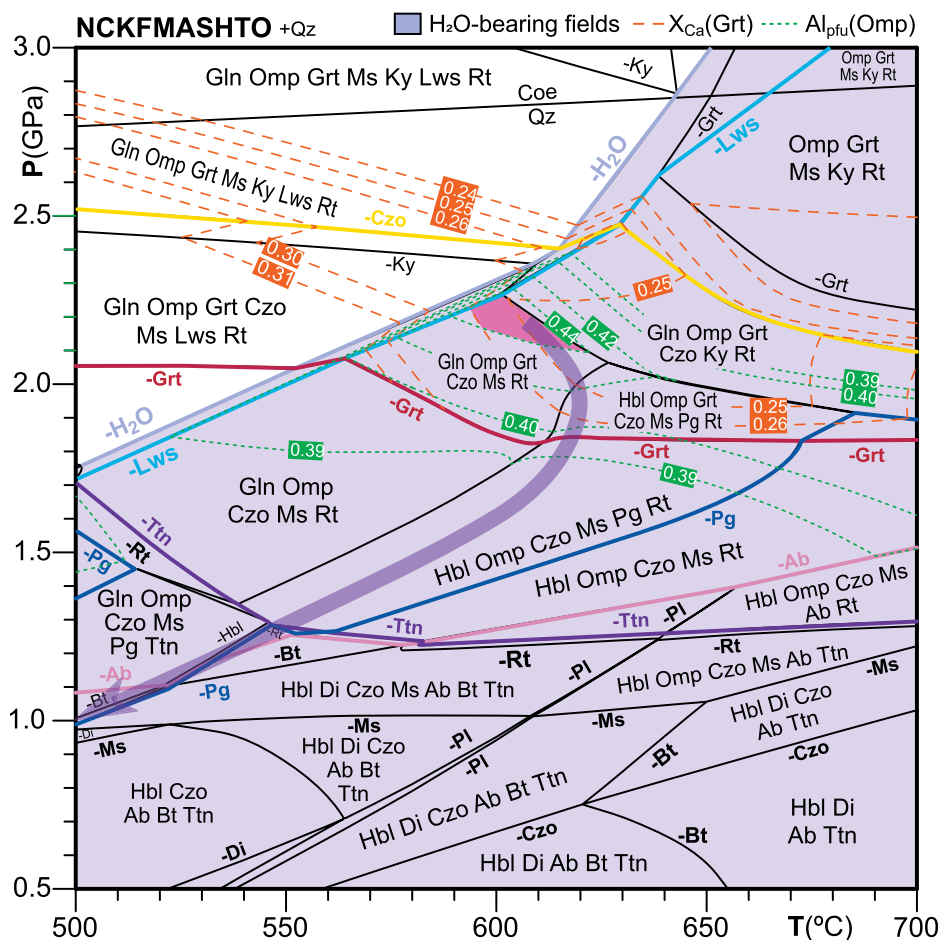
Figure 5. Pressure-temperature (*P-T*) pseudosection with H₂O = 25 mol% calculated for sample T20B from the Shanderman eclogites of NW Iran (SiO₂:55.76; Al₂O₃:20.65; TiO₂:0.75; FeO:6.60; Fe₂O₃:1.37; MgO:10.17; CaO:10.54; Na₂O:8.99; K₂O:0.42). Whole-rock analyses and recalculated proportions are shown in Table 2. Mineral abbreviations are those proposed by Warr (2021). Ab—albite; Bt—biotite; Coe—coesite; Czo—clinozoisite; Di—diopside; Grt—garnet; Gln—glaucophane; Hbl—hornblende; Ky—kyanite; Lws—lawsonite; Ms—muscovite; Omp—omphacite; Pg—paragonite; Pl—plagioclase; Qz—quartz; Rt—rutile; Ttn—titanite; pfu—per formula unit.

Summarizing, the pre-eclogitic paragenesis (S₁) comprises Mn-rich garnet cores (Grt1) together with clinozoisite (Czo) + paragonite (Pg) + rutile (Rt) ± quartz (Qz). The matrix foliation (S₂) records peak paragenesis under eclogitic conditions and encloses Grt2 + omphacite (Omp) + Czo + glaucophane (Gln)/barriosite (Brs) + Pg/muscovite (Ms) + Rt ± Qz. Finally, post-S₂ foliation includes retrogression to amphibolite and greenschist facies conditions shown by distinctive retrograde reaction textures such as symplectites, the replacement of Rt by ilmenite/titanite, Grt2ᵣ re-equilibration, and the late development of carbonate (Fig. 4).

P-T pseudosection calculated for sample T20B is shown in Figure 5. The stability field of the eclogitic assemblage at H₂O-saturated conditions, Gln-Omp-Grt2-Czo-Ms-Rt-H₂O-Qz, is modeled between 1.8 GPa and 2.3 GPa and 565–625 °C. The analyzed content of Al (pfu) in omphacite (Al > 0.39, up to 0.54 pfu) and the grossular content in garnet rim (Grt2ᵣ; $X_{Ca} < 26$) plots in the HP area of the field at 2.1–2.25 GPa and 595–620 °C (Figs. 5 and 6). The pressure-peak paragenesis field is limited by the stability of garnet, lawsonite-bearing assemblages toward high-pressures, and kyanite-bearing assemblages at higher temperatures. The model predicts that the rock crosses the glaucophane-hornblende solvus at slightly lower pressures and higher temperatures (metamorphic peak; 2.0 GPa; 620 °C) to enter in the paragonite-bearing fields, subsequently crossing the garnet-absent domain below 1.8 GPa at

amphibolite facies conditions. The retrograde evolution progresses through the glaucophane-free fields and is constrained by the disappearance of paragonite (that is stable in the whole *P-T* history of sample T20B). Lastly, the rock goes across the albite-bearing fields, rutile disappears, and titanite becomes stable (1.2 GPa; 530 °C). Exhumation progresses in the greenschist facies conditions across the biotite-absent fields toward 1.0 GPa and 500 °C. At rock-slab scale the diagram models peak-conditions and the response of the rock toward lower pressure and temperature (i.e., retrograde conditions). Nevertheless, there are some inconsistencies with petrographic observations. The main irreproducible issue concerns the stability of paragonite in the predicted models. *P-T* pseudosection fails to reproduce the stability of paragonite in the peak assemblage and the appearance of muscovite in the last stages of the retrograde evolution. Despite having calculated different *P-T*-X diagrams considering key components that may affect the stability of white micas and having tried to reproduce this diagram with other classical solid solution models for these phases, the textural relations between muscovite and paragonite cannot be faithfully reproduced. The mode of muscovite versus paragonite is systematically superior in all fields where both coexist, and it is not possible to model a field at high-pressures where only paragonite is stable. Besides the analytical errors associated with electron microprobe analysis or related to the election of the effective domain, the main uncertainties associated with petrologic modeling are due to the thermodynamic data and the a-x (activity-composition) models. Both calibrations determine the reproducibility of natural paragenesis in a model which, from the outset, has many variables that are impossible to constrain (e.g., Powell and Holland, 2008).

The existing solid solution models for white micas in internally consistent databases, used to model phase relationships, accumulate uncertainties. These models have focused on metapelites and are based on calculated experimental data (enthalpy and entropy) and other inferred or estimated thermochemical parameters (e.g., Gibbs free energy or H₂O fugacity) under specific experimental conditions for the paragonite + quartz assemblage (Chatterjee, 1970, 1972). Yet it is assumed that a re-evaluation of the standard enthalpies of muscovite and paragonite, especially in aluminum-rich metapelites, is necessary (Coggon and Holland, 2002). In HP metabasites (eclogites) paragonite would disappear at pressures close to 2.0 GPa by a reaction forming kyanite and omphacite (Holland, 1979), which is what the calcu-
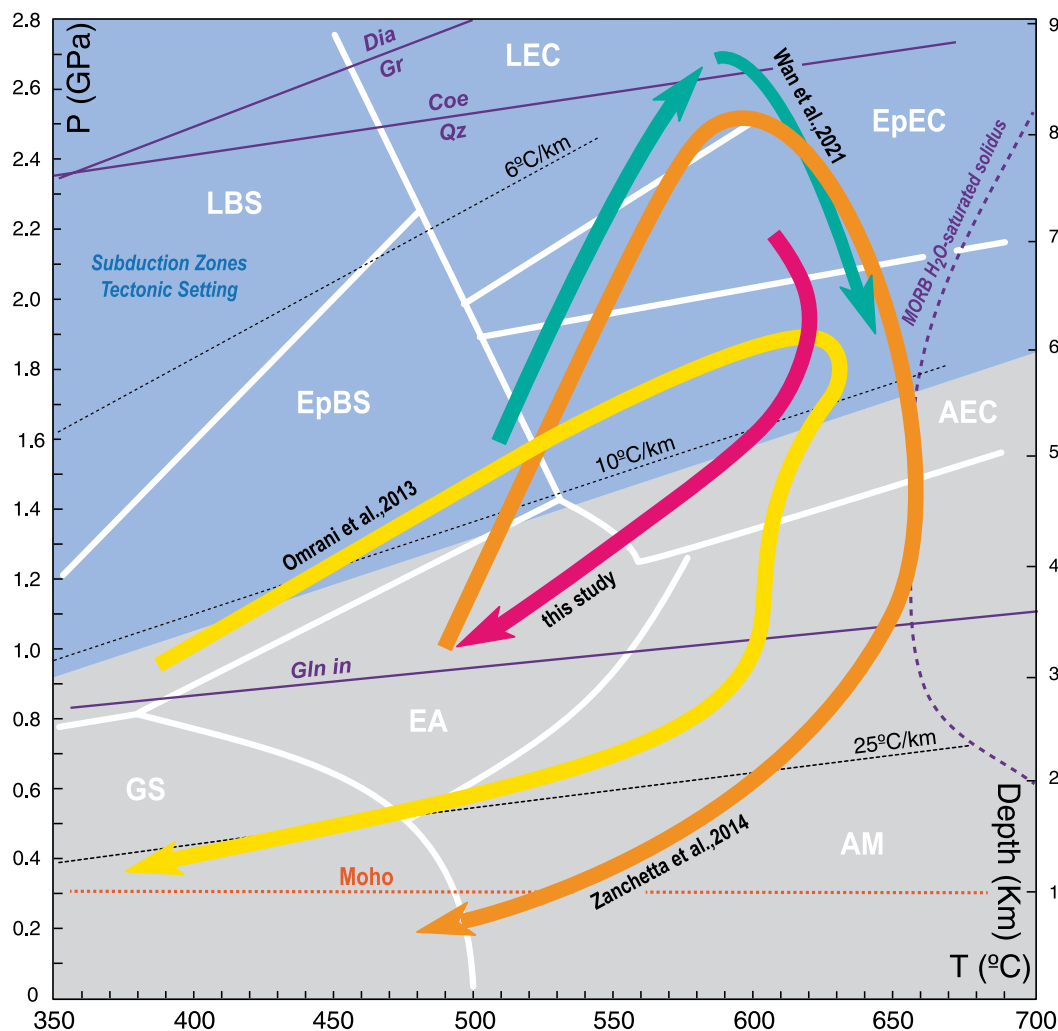
Figure 6. Pressure-temperature (*P-T*) diagram summarizing the proposed paths for the Shanderman eclogites of NW Iran. Diagnostic reactions shown as reference are: diamond (Dia) = graphite (Gr) after Kennedy and Kennedy (1976); coesite (Coe) = quartz (Qz) after Hemingway et al. (1998); glaucophane-in line (denotes the onset of the P-T conditions where Gln is stable in the diagram) after Corona et al. (2013); and H$_2$O saturated solidus for mid-ocean ridge basalt (MORB) (Vielzeuf and Schmidt, 2001). The shallowest Moho after Blackwell (1971) is also included. Metamorphic facies field abbreviations: GS—greenschist; EA—epidote-amphibolite; AM—amphibolite; AEC—amphibole-eclogite; EpBS—epidote blueschist; LBS—lawsonite blueschist; EpEc—epidote eclogite; and LEC—lawsonite eclogite, after Heinrich and Althaus (1988), Evans (1990), Maruyama et al. (1996), and Okamoto and Maruyama (1999).

lated model predicts for these rocks (Fig. 5). The slope of this reaction is highly dependent on the estimated entropy of paragonite, which in turn is related to the poorly known state of A1-Si order in the synthetic albite. Experimental petrology concludes that, in HP assemblages, paragonite is stable in the presence of aqueous fluids (Holland, 1979) at medium temperatures (~550–700 °C; Massonne and Sobiech, 2007). Guidotti et al. (1994) highlighted that the two main controls on the width of the muscovite-paragonite solvus are the silica content in the potassic mica and pressure, whose variation is proportional to the silica content in phengite. The different responses of muscovite and paragonite to increasing pressure are controlled by the Σ(Mg + FeT) (Σ—sumatory) (so called Fm substitution by Guidotti et al., 2000). The incorporation of Fe, Mg, and Si into muscovite is well constrained, and this substitution is accurately calibrated for HP parageneses in a-x models. Nonetheless, the operation of this

substitution in the paragonite is hardly known and any substantial amount of Fm substitution would destabilize it (for a comprehensive description see Guidotti et al., 2000).

3.2. U-Pb and Lu-Hf in Zircon

About 50 kg of eclogite samples were collected in each studied site (T07, T10, T12). Samples were crushed to <500 μm and treated with hydrofluoric acid (Neuerburg, 1961; Oliveira et al., 2022). Zircon grains were hand-picked from the survival mineral phases. In the case of T29 (a quartzite), a 3 kg sample was crushed and zircon crystals were handpicked from the concentrate after panning, heavy liquid separation, and magnetic separation. We obtained one zircon grain from sample T07, one from T10, and 44 from T12. Grains are anhedral or fragmented subhedral and most are <50 μm. Quartzite sample T29 yielded subhedral grains usually over 100 μm, 15 grains presented rims that were large enough to date (see

Supplemental Material[1]). The separated zircon grains were purified by hand-picking under a binocular microscope and mounted with SL13 (U = 238 μg/g; Claoué-Long et al., 1995) and FC-1 (1099 Ma; Paces and Miller, 1993) standard zircon. Back-scattered electron (BSE) and cathodoluminescence (CL) images were obtained using a scanning electron microscope (JEOL JSM-6610LV). The Pb-Th-U isotopes in zircon were analyzed using a sensitive high-resolution ion microprobe (SHRIMP) IIe/MC (Korea Basic Science Institute [KBSI], Seoul, Korea). Selected zircon grains were mounted in epoxy with FC1 (Duluth gabbroic anorthosite, 1099 Ma; Paces and Miller, 1993) and SL13 (Sri Lankan gem zircon; U = 238 μg/g) reference zircons and ground to expose internal
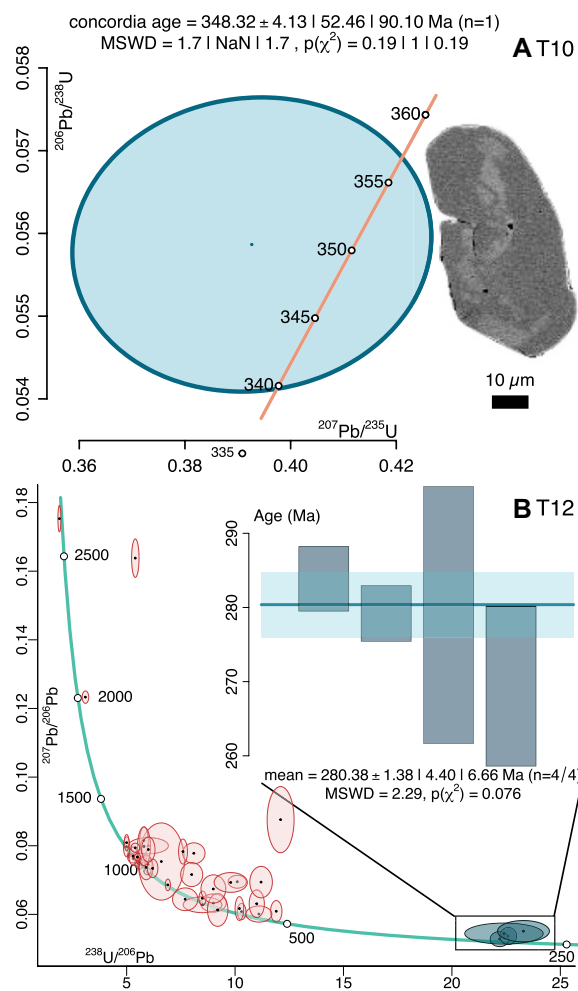
Figure 7. Concordia diagrams for samples T10 (top) and T12 (bottom) of Shanderman eclogites from NW Iran. (A) Cathodoluminescence image of the zircon grain with scale and concordia error for both ellipses. Concordia age is 348.33 ± 4.13 Ma. (B) Concordia diagram for sample T12 where a series of Precambrian inherited zircon grains were found. In addition, the graph shows the mean age of the four Permian grains (in blue), 280.38 ± 1.38 Ma. MSWD—mean square of weighted deviates; n—number of samples.
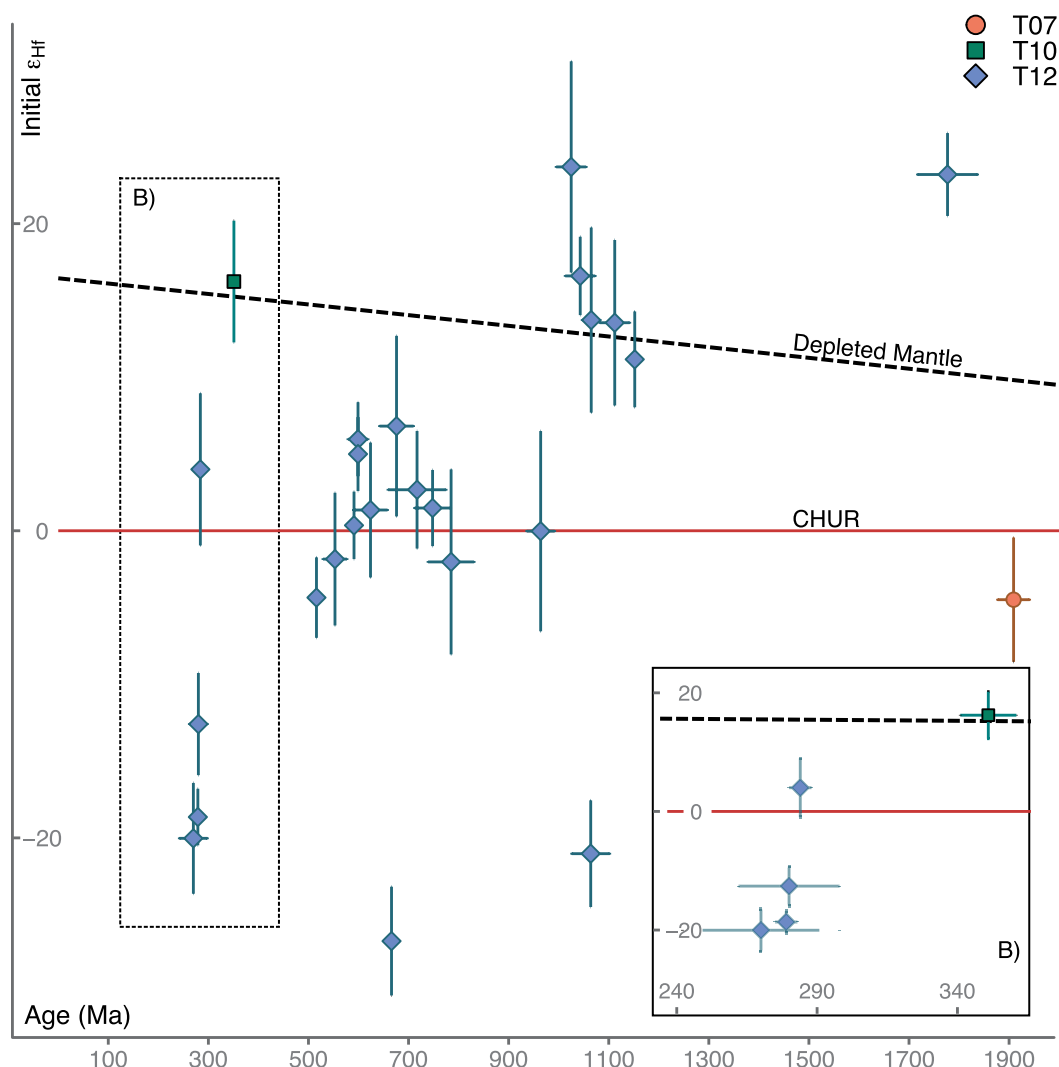
of Chu et al. (2002) and Vervoort et al. (2004), respectively, while mass bias corrections for Hf isotopic ratios were made using an exponential law (^{179}Hf/^{177}Hf = 0.7325; Russell et al., 1978; Patchett, 1983). The ^{176}Lu/^{177}Hf and ^{176}Yb/^{177}Hf ratios were calculated based on the approach by Iizuka and Hirata (2005). To ensure precision and accuracy of the ^{176}Hf/^{177}Hf ratios, reference zircon 91500 (0.282297; Griffin et al., 2000) and Plešovice (0.282482; Sláma et al., 2008) were analyzed repeatedly at the beginning, end, and at regular intervals throughout each session. All ratios were calculated with two standard deviations (2σ error) and data reduction was carried out using Iolite 2.5 software (Paton et al., 2011). The overall analytical procedures, including data acquisition, followed those described in previous studies (e.g., Cheong et al., 2019).

The only zircon in T10 is concordant, with an age of 348.32 ± 4.13 Ma and a very positive εHf signature that plots over the depleted mantle curve (Figs. 7 and 8). T12 shows zircon grains with ages ranging from ca. 280 Ma to <2.5 Ga. The youngest zircon age is a population of four concordant zircon grains whose mean age is 280.38 ± 1.38 Ma (Fig. 7) with variable εHf from very negative ($\sim$−20) to positive values. The spectra of the zircons reveal five peaks of zircon formation, from which three of them (279.4 ± 8.8 Ma; 635.2 ± 99.5 Ma; 1054.2 ± 50.6 Ma) are significant to 90% and two (1956.3 ± 1.7 Ma; 2626.1 ± 1.6 Ma) whose certainty is lower (Fig. 9; see Pastor-Galán et al., 2021). The Ediacaran grains show values of εHf around zero, whereas the peak at 1 Ga shows very positive values (Fig. 8). Sample T07 yielded a single concordant zircon grain with a 1.9 Ga age.

In sample T29 (quartzite) we analyzed 18 zircon grains, 15 grains in both core and rim. Zircon grains provided a spectrum consisting of three populations with a confidence over 90% (625.6 ± 25.7 Ma, confidence: 96%; 999.7 ± 48.3 Ma, confidence: 100%; and 1998.8 ± 34.4 Ma, confidence: 95%). In some cases, rims and cores yielded the same ca. 650 Ma ages. In other cases, cores provided from 2.2 Ga to 2.9 Ga, whereas their rims yielded ca. 2.0 Ga (Supplemental Material).

3.3. Sm-Nd Isochron

Samples from three different eclogitic samples (T07, T20, and T20b) where crushed and separated in a whole rock fraction, garnet, mafic (pyroxene + amphibole), and mica (phengite + paragonite). Whole rock powders were accurately weighed and totally spiked with a known amount of mixed ^{150}Nd-^{149}Sm tracer solution—this tracer is calibrated directly against the Caltech mixed Sm/Nd

zones. Before analysis, the grains were photographed with an optical microscope, and their internal zoning was imaged by CL and BSE using a JEOL JSM-6610LV scanning electron microscope at KBSI. SHRIMP analysis follows the protocols described in Williams (1998). A 3.0–4.0 nA mass filtered O_2-primary beam was focused on a spot of $\sim$20 μm diameter on the polished surface of each target zircon grain. Each spot was rastered with the primary beam for $\sim$3 min prior to the analysis and then analyzed five cycles with a single electron multiplier. During one cycle, the magnet was stepped through nine peaks of ^{90}Zr$_2$^{16}O (counting time = 2 s), ^{204}Pb (10 s), ^{206}Pb (20 s), ^{207}Pb (40 s), ^{208}Pb (10 s), ^{238}U (5 s), ^{232}Th^{16}O (2 s), and ^{238}U16O (2 s) and 204.1 (10 s; background position). Data processing was conducted using SQUID 2.50 (Ludwig, 2009) and the concordia plots produced using Isoplot 3.75 (Ludwig, 2012) programs, running under Excel 2003. Weighted mean ages of zircons were calculated using ^{207}Pb-corrected ^{206}Pb/^{238}U ratios after excluding outliers under statistical t-test and reported

at 95% confidence. Common Pb was removed following the ^{207}Pb (for dates <1000 Ma) or ^{204}Pb (for dates >1000 Ma) correction method using the model by Stacey and Kramers (1975). Ages and concordia diagrams were calculated with IsoplotR (Vermeesch, 2018) and population statistics with BAD-ZUPA, a Bayesian approach for evaluating detrital zircon U-Pb ages (Pastor-Galán et al., 2021).

Lu-Hf isotope analyses were performed on zircon grains from eclogitic samples (T07, T10, T12) using a laser ablation system coupled to a Nu Plasma II multi-collector–inductively coupled plasma–mass spectrometer (LA-MC-ICP-MS) at KBSI. The Lu-Hf isotopic compositions were measured on the same zircon grains used for U-Pb age determinations. Helium (650 mL/min) and nitrogen (2 mL/min) were used as carrier gases to enhance Hf isotope intensity, with an energy density of 6–8 J/cm^2 (Iizuka and Hirata, 2005). The laser spot size was 50 μm in diameter, with a repetition rate of 10 Hz. Corrections for ^{176}Lu and ^{176}Yb interference on the ^{176}Hf signal were applied following the methods

Figure 8. εHf in zircon grains in respect to their U-Pb zircon age for the Shanderman eclogites from NW Iran. Zircon with U-Pb ages of ca. 1.1 Ga show very juvenile εHf whereas those with Ediacaran and Cryogenian ages show less juvenile signatures and mixing. The Carboniferous zircon from T10 has a depleted mantle εHf signature suggesting it was extracted from a mid-oceanic ridge. The Permian zircon of sample T12 show a large variety of εHf signatures implying mixing between juvenile and older crustal sources is a setting that can occur, for example, in a continental arc. CHUR—chondritic uniform reservoir.

normal described by Wasserburg et al. (1981). Dissolution occurred in mixed 24N HF + 16N HNO_3 media in sealed Teflon™ PFA vessels at 160 °C for six days. The fluoride residue was converted to chloride with HCl, and Nd and Sm were separated by conventional cation and Bis(2-ethylhexyl)phosphoric acid-based chromatography. Chemical processing blanks of <200 picograms of either Sm or Nd were used, an insignificant amount relative to the amount of Sm or Nd analyzed for any rock sample. Further details can be found in Creaser et al. (1997) and Unterschutz et al. (2002).

The isotopic composition of Nd is determined in static mode by MC-ICP-MS (Schmidberger et al., 2007). All isotope ratios are normalized for variable mass fractionation to a value of $^{146}Nd/^{144}Nd = 0.7219$ using the exponential fractionation law. The $^{143}Nd/^{144}Nd$ ratio of samples is presented here relative to a value of 0.511850 for the LaJolla Nd isoto-

pic standard, monitored by use of an in-house Alfa Nd isotopic standard for each analytical session. Sm isotopic abundances are measured in static mode by MC-ICP-MS and are normalized for variable mass fractionation to a value of 1.17537 for $^{152}Sm/^{154}Sm$ also using the exponential law. Using the same isotopic analysis and normalization procedures above, we analyze the Geological Survey of Japan Nd isotope standard "Shin Etsu: J-Ndi-1" (Tanaka et al., 2000), which has a $^{143}Nd/^{144}Nd$ value of 0.512107 ± 7 relative to a LaJolla $^{143}Nd/^{144}Nd$ value of 0.511850, when normalized to $^{146}Nd/^{144}Nd = 0.7219$. The value of $^{143}Nd/^{144}Nd$ determined for the JNdi-1 standard conducted during the analysis of the samples reported here was 0.512081 ± 6 (two standard deviations); the long-term average value is 0.512095 ± 8 (one standard deviation, n = 7, past year). Using the mixed ^{150}Nd-^{149}Sm tracer, the measured $^{147}Sm/^{144}Nd$ ratios for the international rock standard BCR-1 range from

0.1380 to 0.1382, suggesting reproducibility for $^{147}Sm/^{144}Nd$ of $\sim\pm$ 0.1% for real rock powders. The value of $^{147}Sm/^{144}Nd$ determined for BCR-1 is within the range of reported literature values by isotope dilution methods.

Sm-Nd isochrons were calculated with IsoplotR (Vermeesch, 2018). As expected for eclogites, individual sample isochrons are controlled by garnet, because it strongly fractionates Sm over Nd leaving the other fractions very depleted in Sm (Supplemental Material). T07 yielded a low-resolution isochron of 379.97 ± 9.97 Ma, whereas T20 (346.31 ± 3.97 Ma) and T20b (348.39 ± 3.60 Ma) provided somewhat more accurate isochrons, but still face the problem of Sm fractionation in garnet (Supplemental Material). A combination of samples T20 and T20b (collected from two boulders in the same site) yields two distinct points for garnets that show a linear relationship with the rest of fractions providing a robust isochron of 350.50 ± 5.08 Ma (Fig. 10).
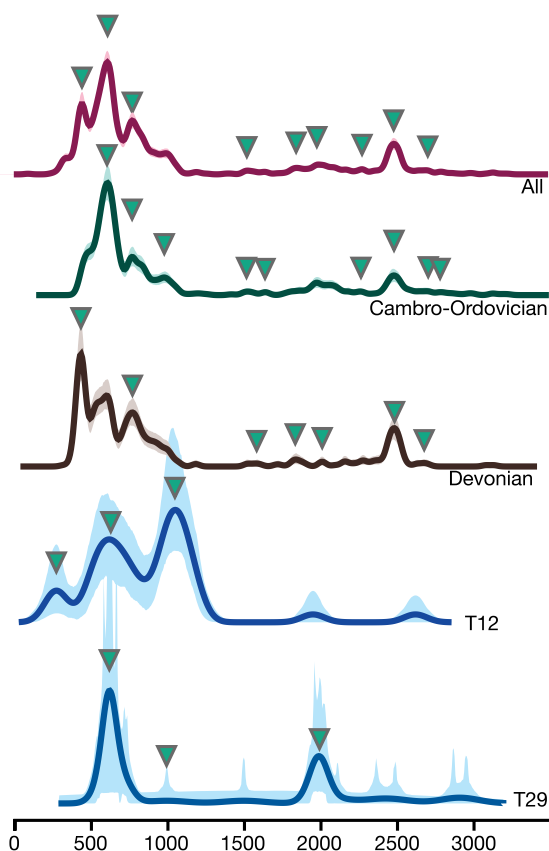
Figure 9. Relationship between the detrital signature of the inherited zircon grains of sample T12 and the metasandstone quartzite sample T29 from Shanderman eclogites, NW Iran (Horton et al., 2008; Honarmand et al., 2018; Moghadam et al., 2017).

4. DISCUSSION

4.1. Nature of the Shanderman Eclogites

The Shanderman eclogite's geochemical features are consistent with basalts, gabbros, and peridotites generated possibly in a mid-oceanic ridge (e.g., Zanchetta et al., 2009; Omrani et al., 2013; Wan et al., 2021). This segment of oceanic crust subducted until reaching eclogite conditions. Previous studies suggested various *P-T*-time paths (Fig. 6). All of them approximately agree on the peak temperature (∼620 °C) but significantly differ in the maximum P: from the 1.8 GPa (Omrani et al., 2013) to 2.7 GPa (Wan et al., 2021). Following the model prediction, we propose that these eclogites subducted at H_2O-saturated conditions up to <80 km (2.1–2.25 GPa) following a typical *P-T* trend of a cold subduction zone, reaching the ∼600 °C isograd characteristic of LT eclogites. From that depth, the studied pieces of eclogite began its way back to the surface crossing the glaucophane-hornblende solvus at ∼2 GPa and reaching its peak temperature (625 °C), before entering the paragonite-bearing fields. The rock then transitioned into garnet-free fields below 1.8 GPa under amphibolite-facies conditions. Subsequently, the rock crosses the albite-bear-ing fields, where rutile vanishes and titanite becomes stable (1.2 GPa, 530 °C). Eventually exhumation arrives to greenschist-facies conditions, passing through biotite-absent fields (∼1.0 GPa, 500 °C).

4.2. Significance of U-Pb, Lu-Hf, and Sm-Nd Ages

Zircon is scarce or absent from mid-ocean ridge rocks, and despite 50 kg of rock collected from sites T07, T10, and T12, we retrieved only 46 zircon grains: 41 show Proterozoic ages (Figs. 7–9), 44 were found in sample T12. The small and fragmented zircon grains in samples T12 and T07 reveal two Proterozoic populations (635.2 ± 19.5 Ma; 1054.2 ± 50.5 Ma) and four Permian grains (277.5 ± 48.8 Ma). The occurrence of Proterozoic zircon indicates either (1) the presence of pieces of continental crust embedded in the oceanic crust as observed in the present day Indian Ocean (e.g., Ashwal et al., 2017) or (2) a detrital zircon source located relatively close to a spreading ridge at some point. The main inherited zircon populations in samples T12 and T29 are quite similar. In addition, both samples resemble other detrital zircon units studied in NW Iran (e.g., Fig. 7; Horton et al., 2008; Honarmand et al., 2018; Moghadam et al., 2017). We think that the Cadomian arc terranes along the northern margin of Gondwana (e.g., Fernández-Suárez et al., 2014; Avigad et al., 2018; Azor et al., 2021), particularly in NW Iran (Moghadam et al., 2017; Honarmand et al., 2018), are a potential source of the inherited zircons found in the Shanderman eclogites. However, we recognize the limitations of our data set in identifying the source of these inherited grains.

The Shanderman eclogites also yielded five late Paleozoic zircon grains. The only zircon from sample T10 (Fig. 7) shows an Early Carboniferous age (348.32 ± 4.13 Ma) and an εHf of 16 ± 4, which plots above the depleted mantle curve (Fig. 8). This suggests that the zircon crystallized directly from a depleted mantle source. The Sm-Nd isochron calculated from samples T20 and T20b yielded an age of 350.50 ± 5.08 Ma (Fig. 10), consistent with the peak metamorphism ages (phengite $^{40}Ar/^{39}Ar$ and rutile U-Pb) obtained by Wan et al. (2021) and Rossetti et al. (2017) in the Shanderman and Asalem complexes. The εNd values range between 7 and 11, which plots over the depleted mantle curve and supports a MORB protolith. There is an agreement in age between the T10 zircon grain and the Sm-Nd and other ages interpreted as corresponding to peak metamorphism (Rossetti et al., 2017; Wan et al., 2021). Despite this age coincidence, we interpret that the T12 zircon age might represent the crystallization age of the oceanic crust. Zircon stability in metamorphic rocks is (1) strongly temperature-dependent and (2) influenced by the presence of common phases in eclogites, such as garnet, which incorporates increasing amounts of Zr as the temperature increases, leading to the resorption of coexisting zircon (Degeling et al., 2001). Our temperature estimates suggest retrograde conditions below 630 °C, which is insufficient for the crystallization of new zircon from slab-derived dehydration fluids (Chen and Zheng, 2017). While recrystallization during HP metamorphism cannot be entirely ruled out, preserved zircon core fragments typically retain either original concordant ages or exhibit discordance. In fact, none of the inherited zircon grains in the Shanderman eclogites show any evidence of metamorphic rims or regrowths (Supplemental Material), supporting the absence of newly formed zircon during peak metamorphism. If the zircon age indeed reflects the oceanic crustal age, this would suggest that subduction occurred shortly after the formation of this oceanic crust, given the likely 5–10 m.y. required to reach the 60–70 km depth at which the Shanderman eclogites formed.

The four Paleozoic zircons in sample T12 show Permian ages (ca. 280 Ma; Figs. 7–9), and their εHf values are variable, indicating a mixed crustal origin. The 280 Ma zircon grains
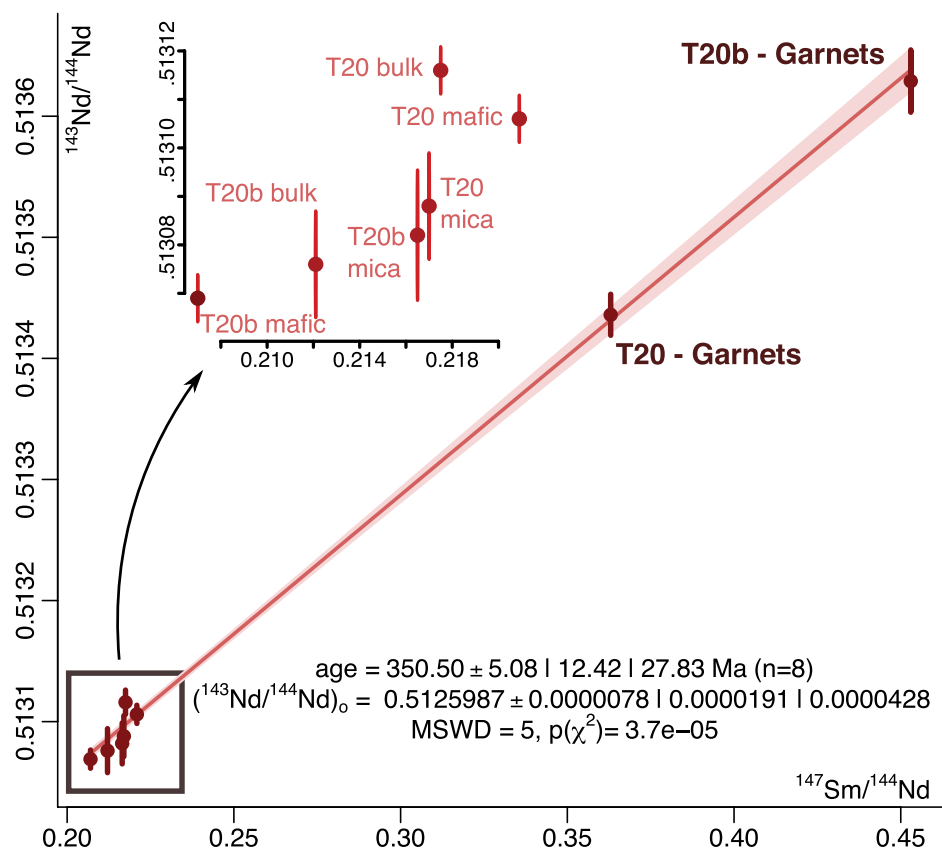
Figure 10. Sm-Nd Isochron obtained from samples T20 and T20b from Shanderman eclogites, NW Iran (collected in two blocks within the same outcrop). The isochron was obtained separating the micas, mafic minerals, and garnet phases and plotting all of them along the bulk rock. The age (350.5 ± 5.08 Ma) is largely coincident with $^{40}Ar/^{39}Ar$ in blueschists (Rossetti et al., 2017) and rutile U-Pb isochron in the same rocks (Wan et al., 2021). MSWD—mean square of weighted deviates; n—number of samples.

from sample T12 are fractured but concordant. Their ages coincide with the lower temperature $^{40}Ar/^{39}Ar$ ages in phengite obtained by Rossetti et al. (2017) from the Asalem metabasites (being the higher T at ca. 350 Ma). Following Rossetti et al.'s interpretation of a Permian overprint, we propose that hydrothermal activity could explain the resetting of $^{40}Ar/^{39}Ar$ ages and the crystallization of zircon (e.g., Schaltegger, 2007).

4.3. A Tectonic Scenario for the HP Rocks of NW Iran

We have tentatively adapted the kinematic reconstructions of Domeier (2016), Domeier and Torsvik (2014), and Pastor-Galán (2022) to incorporate the events documented in the Pontide-Kopeh Dagh belt (e.g., Rolland et al., 2016; Vasey et al., 2020; Wan et al., 2021). During the Cambrian and Ordovician, a diachronic transition occurred from Cadomian arc activity to the opening of the Rheic ocean (Fig. 11; Nance et al., 2010). In Ordovician–Silurian times, the Pontide-Kopeh Dagh margin of Gondwana drifted away, forming the Paleotethyan ocean as the terrane migrated northward (e.g., Domeier, 2016; Domeier and Torsvik, 2014). The Transcaucasus region provides evidence of igneous activity from the Cadomian arc spanning 700–400 Ma (Rolland et al., 2016; Akdoğan et al., 2021). This, along with the presence of igneous and high-temperature rocks, suggests a southward-directed subduction of the Rheic ocean beneath the Pontide-Kopeh Dagh system (Rolland et al., 2016). The Pontide-Kopeh Dagh likely acted as a ribbon continent that rifted from Gondwana at ca. 460 Ma, shortly after Cadomian arc activity ceased in most regions but persisted in this terrane (e.g., Rolland et al., 2016; Vasey et al., 2020; Akdoğan et al., 2021). The simplest explanation for the drift of the Pontide-Kopeh Dagh Cadomian arc is the roll-back of the subducting slab (Fig. 11). The mechanism behind this rapid process may involve one or several of the following: the "infection" of subduction into the Rheic ocean (e.g., Rolland et al., 2016; Vasey

et al., 2020), slab-pull associated with ridge subduction of the Rheic ocean (e.g., Gutiérrez-Alonso et al., 2008a), or subduction initiation along or near the Rheic mid-ocean ridge. The oceanic rocks of the Rasht complex (Shanderman and Asalem) reached peak eclogitic conditions at ca. 350 Ma, as confirmed by consistent $^{40}Ar/^{39}Ar$ dating in micas (Rossetti et al., 2017; Wan et al., 2021), U-Pb isochron dating in rutile (Wan et al., 2021), and Sm-Nd isochron data from this study. Rossetti et al. (2017) pointed out that this subduction zone represents the oldest known along the suture zones of the putative Palaeotethys, contrasting with the more common Permian–Triassic ages reported from this region (e.g., Bagheri and Stampfli, 2008; Rolland et al., 2016). In light of this, we argue that the Rasht metamorphic units are likely relics of the Rheic ocean, rather than remnants of the Paleotethys ocean or its basins (Figs. 11 and 12). It is also plausible that part of the oceanic crust that subducted beneath the Pontide-Kopeh Dagh belt formed immediately before the onset of subduction, a scenario that could involve either subduction initiation along a mid-oceanic ridge or ridge subduction. Although we lack definitive evidence to support one scenario over the other, if the migration of the Pontide-Kopeh Dagh ribbon continent over a subduction zone is accurate (Figs. 11 and 12; e.g., Rolland et al., 2016; Vasey et al., 2020; Akdoğan et al., 2021), we favor the ridge subduction hypothesis.

During the Late Devonian to Early Mississippian, the closure of the Rheic and its associated basins between Laurussia and Gondwana (e.g., Domeier and Torsvik, 2014; Wu et al., 2021) culminated in the collision that formed Pangea to the west (Stampfli et al., 2013; Weil et al., 2013). The Pontide-Kopeh Dagh onset of the collision could have been recorded at ca. 330–320 Ma by the metamorphism in the Allahyarlu and Anarak complexes (Bagheri and Stampfli, 2008; Moazzen et al., 2020). Younger zircon (ca. 280 Ma), though fractured, remain concordant and are interpreted as hydrothermal in origin, likely related to the onset of Paleotethyan subduction (e.g., Pastor-Galán, 2022). These zircon ages suggest that by the Early Permian, the Rasht complex was part of the subduction system beneath Eurasia, rather than Gondwana, as indicated by the lack of arc-related magmatism and the presence of intraplate activity in Alborz and Cimmerian Iran (e.g., Delavari et al., 2016).

5. CONCLUSIONS

(1) The Shanderman eclogites' protoliths were mid-oceanic ridge basalt that underwent peak metamorphism at a maximum pressure of 2.25 GPa.
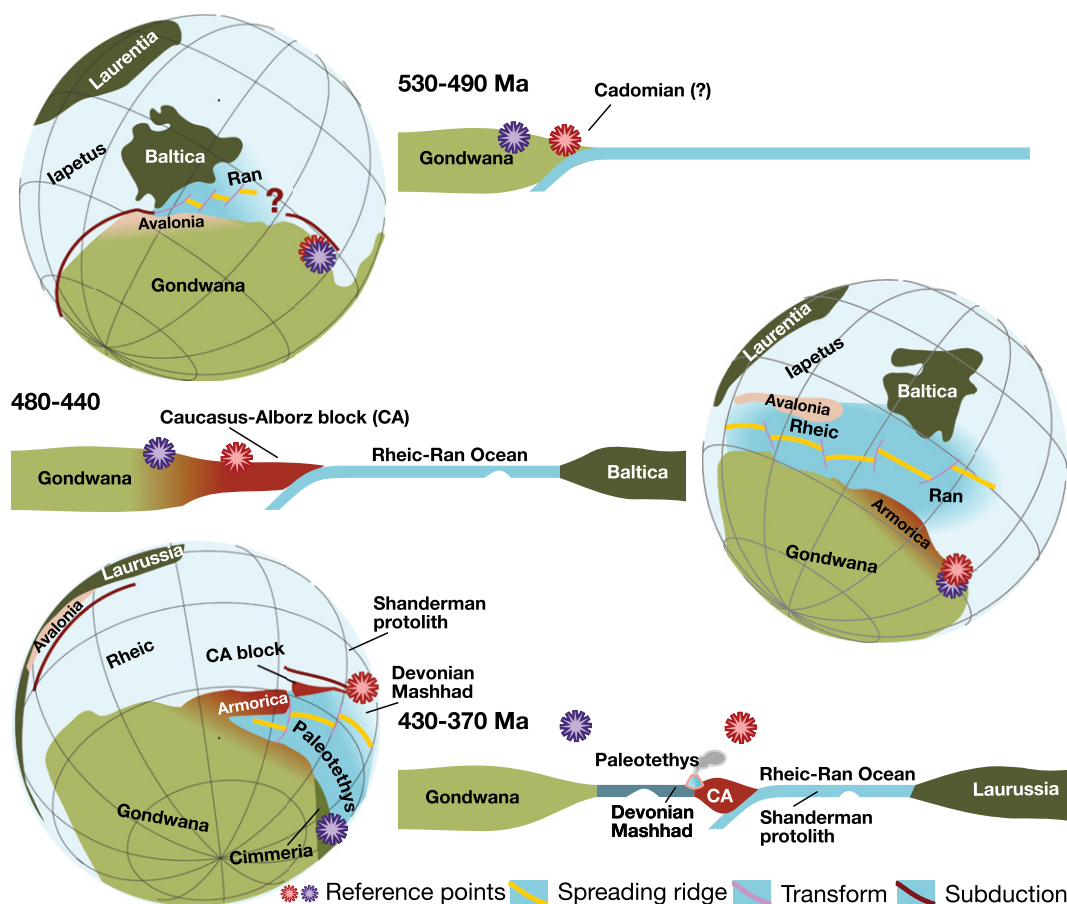
Figure 11. Proposed Cambrian to Devonian tectonic and paleogeographic evolution of the Caucasus-Alborz region. During the Ediacaran to Early Ordovician, the Caucasus-Alborz block was part of the Cadomian arc, a large continental arc and accretionary orogen along Gondwana's margin. Unlike its western counterpart, the subduction responsible for the Ediacaran Cadomian arc continued beneath the Caucasus-Alborz terrane throughout the Ordovician (see text for details). During the Silurian and Devonian, the Paleotethys opened as a triangular ocean, separating the Armorica composite ribbon continent from the Gondwanan margin. The Caucasus-Alborz likely represents the easternmost extent of this continent.

(2) Peak metamorphism occurred at ca. 350 Ma (Sm-Nd isochron in garnet), making it the oldest recorded for the Paleotethys, but consistent with the metamorphism found in the Rheic/Ran/Prototethys oceans.

(3) We speculate that the single zircon U-Pb and Lu-Hf age (348.32 ± 4.13 Ma, $\varepsilon Hf = 16 \pm 4$) indicates that the oceanic crust formed immediately before subduction and metamorphism.

(4) The inherited zircon grains found suggest that the protolith formed in proximity of a Gondwana-derived terrane, either as a source of sediment in the overriding plate or as a sliver of continent embedded in the ocean.

(5) The Rasht HP metamorphic rocks (Shanderman and Asalem complexes) likely represent the Rheic/Ran/Prototethys oceans rather than the Paleotethys.

(6) Zircon grains with ages of 280 Ma suggest that after the Carboniferous collision of the Pontide-Kopeh Dagh terrane, the Paleotethys began subducting beneath Eurasia.

REFERENCES CITED

Akdoğan, R., Hu, X., Okay, A.I., Topuz, G., and Xue, W., 2021, Provenance of the Paleozoic to Mesozoic siliciclastic rocks of the Istanbul Zone constrains the timing of the Rheic Ocean closure in the Eastern Mediterranean region: Tectonics, v. 40, no. 12, https://doi.org/10.1029/2021TC006824.

Alavi, M., 1991, Sedimentary and structural characteristics of the Paleo-Tethys remnants in northeastern Iran: Geological Society of America Bulletin, v. 103, p. 983–992, https://doi.org/10.1130/0016-7606(1991)103<0983:SASCOT>2.3.CO;2.

Alavi, M., 1996, Tectonostratigraphic synthesis and structural style of the Alborz mountain system in Northern Iran: Journal of Geodynamics, v. 21, p. 1–33, https://doi.org/10.1016/0264-3707(95)00009-7.

Ashwal, L.D., Wiedenbeck, M., and Torsvik, T.H., 2017, Archaean zircons in Miocene oceanic hotspot rocks establish ancient continental crust beneath Mauritius: Nature Communications, v. 8, 14068, https://doi.org/10.1038/ncomms14086.

Avigad, D., Rossi, P., Gerdes, A., and Abbo, A., 2018, Cadomian metasediments and Ordovician sandstone from Corsica: Detrital zircon U-Pb-Hf constrains on their provenance and paleogeography: International Journal of Earth Sciences, v. 107, p. 2803–2818, https://doi.org/10.1007/s00531-018-1629-3.

Azor, A., Poyatos, D.M., Accotto, C., Simancas, F., Lodeiro, F.G., Talavera, C., and Evans, N.J., 2021, Transcurrent displacement of the Cadomian magmatic arc: Precambrian Research, v. 361, https://doi.org/10.1016/j.precamres.2021.106251.
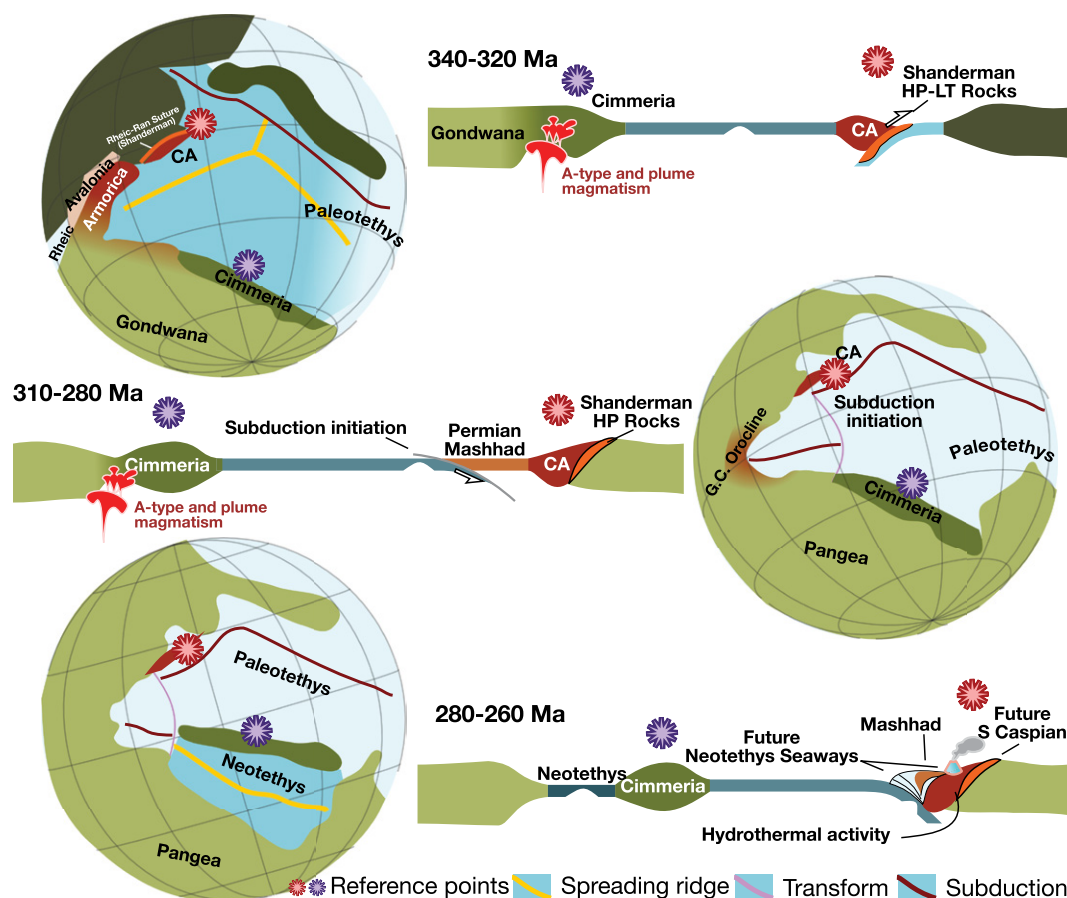
Figure 12. Tectonic evolution during the Carboniferous: expansion of the Paleotethys and Rheic-Ran consumption. In the Early Carboniferous (ca. 350 Ma), a segment of the subducting Rheic-Ran ocean (the Shanderman eclogite of NW Iran) was exhumed and emplaced. During the Carboniferous, the collision between Armorica, Laurussia, and Gondwana in the west resulted in the formation of the Variscan-Alleghanian orogen. In its later stages, this orogeny experienced a plate reorganization (e.g., Pastor-Galán, 2022), which initiated Paleotethys subduction beneath the Eurasian margin and contributed to the formation of the Greater Cantabrian Orocline. The slab-pull from Paleotethyan subduction, possibly assisted by plume volcanism along Gondwana's margin, facilitated the opening of the Neotethys ocean during the Permian. CA—Caucasus-Alborz block.

Bagheri, S., and Stampfli, G.M., 2008, The Anarak, Jandaq and Posht-e-Badam metamorphic complexes in central Iran: New geological data, relationships and tectonic implications: Tectonophysics, v. 451, no. 1–4, p. 123–155, https://doi.org/10.1016/j.tecto.2007.11.047.

Berberian, M., and King, G.C.P., 1981, Towards a paleogeography and tectonic evolution of Iran: Canadian Journal of Earth Sciences, v. 18, no. 2, p. 210–265, https://doi.org/10.1139/e81-019.

Blackwell, D.D., 1971, The thermal structure of the continental, *in* Heacock, J.G., and Blackwell, D.D., eds., The Structure and Physical Properties of the Earth's Crust: American Geophysical Union, Geophysical Monograph Series, v. 14, p. 169–184, https://doi.org/10.1029/GM014p0169.

Chatterjee, N.D., 1970, Synthesis and upper stability of paragonite: Contributions to Mineralogy and Petrology, v. 27, p. 244–257, https://doi.org/10.1007/BF00385781.

Chatterjee, N.D., 1972, The upper stability limit of the assemblage paragonite + quartz and its natural occurrences: Contributions to Mineralogy and Petrology, v. 34, p. 288–303, https://doi.org/10.1007/BF00373759.

Chen, R.X., and Zheng, Y.F., 2017, Metamorphic zirconology of continental subduction zones: Journal of Asian Earth Sciences, v. 145, p. 149–176, https://doi.org/10.1016/j.jseaes.2017.04.029.

Cheong, A.C.S., Jeong, Y.J., Lee, S., Yi, K., Jo, H.J., Lee, H.S., Park, C., Kim, N.K., Li, X.H., and Kamo, S.L., 2019, LKZ-1: A new zircon working standard for the in situ determination of U-Pb age, O-Hf isotopes, and trace element composition: Minerals (Basel), v. 9, no. 5, https://doi.org/10.3390/min9050325.

Chu, N.-C., et al., 2002, Hf isotope ratio analysis using multi-collector inductively coupled plasma mass spectrometry: An evaluation of isobaric interference corrections: Journal of Analytical Atomic Spectrometry, v. 17, no. 12, p. 1567–1574, https://doi.org/10.1039/b206707b.

Clark, G.C., Davies, R.G., Hamzepour, G., and Jones, C.R., 1975, Explanatory Text of the Bandar-e-Pahlavi Quad-

rangle Map, 1:250,000: Tehran, Iran, Geological Survey of Iran, 198 p.

Claoué-Long, J.C., Compston, W., Roberts, J., and Fanning, C.M., 1995, Two Carboniferous ages: A comparison of SHRIMP zircon dating with conventional zircon ages and ^{40}Ar/^{39}Ar analysis, *in* Berggren, W.A., Kent, D.V., Aubry, M.-P., and Hardenbol, J., eds., Geochronology, Time Scales and Global Stratigraphic Correlation: SEPM (Society for Sedimentary Geology), v. 54, https://doi.org/10.2110/pec.95.04.0003.

Coleman, R.G., Lee, D.E., Beatty, L.B., and Brannock, W.W., 1965, Eclogites and eclogites: Their differences and similarities: Geological Society of America Bulletin, v. 76, p. 483–508, https://doi.org/10.1130/0016-7606(1965)76[483:EAETDA]2.0.CO;2.

Coggon, R., and Holland, T.J.B., 2002, Mixing properties of phengitic micas and revised garnet-phengite thermobarometers: Journal of Metamorphic Geology, v. 20, no. 7, p. 683–696, https://doi.org/10.1046/j.1525-1314.2002.00395.x.

Corona, J.C., Jenkins, D.M., and Holland, T.J., 2013, Constraints on the upper pressure stability of blueschist facies metamorphism along the reaction: Glaucophane = talc + 2 jadeite in the Na_2O-MgO-Al_2O_3-SiO_2-H_2O system: American Journal of Science, v. 313, no. 10, p. 967–995, https://doi.org/10.2475/10.2013.01.

Crawford, A., 1977, A Summary of Isotopic age data for Iran Pakistan and India: Mémoires de la Société Géologique de France, v. 8, p. 251–260.

Creaser, R.A., Erdmer, P., Stevens, R.A., and Grant, S.L., 1997, Tectonic affinity of Nisutlin and Anvil assemblage strata from the Teslin tectonic zone, northern Canadian Cordillera: Constraints from neodymium isotope and geochemical evidence: Tectonics, v. 16, p. 107–121, https://doi.org/10.1029/96TC03317.

de Capitani, C., and Brown, T.H., 1987, The computation of chemical equilibrium in complex systems containing non-ideal solutions: Geochimica et Cosmochimica

Acta, v. 51, p. 2639–2652, https://doi.org/10.1016/0016-7037(87)90145-1.

de Capitani, C., and Petrakakis, K., 2010, The computation of equilibrium assemblage diagrams with Theriak/Domino software: American Mineralogist, v. 95, p. 1006–1016, https://doi.org/10.2138/am.2010.3354.

Degeling, H., Eggins, S., and Ellis, D.J., 2001, Zr budgets for metamorphic reactions, and the formation of zircon from garnet breakdown: Mineralogical Magazine, v. 65, no. 6, p. 749–758, https://doi.org/10.1180/0026461016560006.

Delavari, M., Dolati, A., Marroni, M., Pandolfi, L., and Saccani, E., 2016, Association of MORB and SSZ ophiolites along the shear zone between Coloured Mélange and Bajgan Complexes (North Maran, Iran): Evidence from the Sorkhband area: Ofioliti, v. 41, p. 21–34.

Dewey, J.F., and Burke, K.C., 1973, Tibetan, Variscan, and Precambrian basement reactivation: Products of continental collision: The Journal of Geology, v. 81, no. 6, p. 683–692, https://doi.org/10.1086/627920.

Dietz, R.S., and Holden, J.C., 1970, Reconstruction of Pangaea: Breakup and dispersion of continents, Permian to present: Journal of Geophysical Research, v. 75, no. 26, p. 4939–4956, https://doi.org/10.1029/JB075i026p04939.

Domeier, M., 2016, A plate tectonic scenario for the Iapetus and Rheic Oceans: Gondwana Research, v. 36, p. 275–295, https://doi.org/10.1016/j.gr.2015.08.003.

Domeier, M., and Torsvik, T.H., 2014, Plate tectonics in the late Paleozoic: Geoscience Frontiers, v. 5, p. 303–350, https://doi.org/10.1016/j.gsf.2014.01.002.

Domeier, M., and Torsvik, T.H., 2019, Full-plate modelling in pre-Jurassic time: Geological Magazine, v. 156, p. 261–280, https://doi.org/10.1017/S0016756817001005.

Evans, B.W., 1990, Phase relations of epidote-blueschists: Lithos, v. 25, p. 3–23.

Fernández-Suárez, J., et al., 2014, The Ediacaran–Early Cambrian detrital zircon record of NW Iberia: Possible sources and paleogeographic constraints: International Journal of Earth Sciences, v. 103, p. 1335–1357, https://doi.org/10.1007/s00531-013-0923-3.

Ganbat, A., Pastor-Galán, D., Hirano, N., Nakamura, N., Sumino, H., Yamaguchi, Y., and Tsujimori, T., 2021, Cretaceous to Miocene NW Pacific Plate kinematic constraints: Paleomagnetism and Ar-Ar geochronology in the Mineoka Ophiolite Mélange (Japan): Journal of Geophysical Research: Solid Earth, v. 126, https://doi.org/10.1029/2020JB021492.

Green, E.C.R., White, R.W., Diener, J.F.A., Powell, R., Holland, T.J.B., and Palin, R.M., 2016, Activity-composition relations for the calculation of partial melting equilibria in metabasic rocks: Journal of Metamorphic Geology, v. 34, p. 845–869, https://doi.org/10.1111/jmg.12211.

Griffin, W.L., Pearson, N.J., Belousova, E., Jackson, S.V., Van Achterbergh, E., O'Reilly, S.Y., and Shee, S.R., 2000, The Hf isotope composition of cratonic mantle: LAM-MC-ICPMS analysis of zircon megacrysts in kimberlites: Geochimica et Cosmochimica Acta, v. 64, p. 133–147, https://doi.org/10.1016/S0016-7037(99)00343-9.

Guan, Q., Liu, Y., Neubauer, F., Li, S., Genser, J., Yuan, S., Chang, R., Huang, Q., and Fang, Q., 2021, Opening of the West Paleo-Tethys Ocean: New insights from earliest Devonian meta-mafic rocks in the Saualpe crystalline basement, Eastern Alps: Gondwana Research, v. 97, p. 121–137, https://doi.org/10.1016/j.gr.2021.05.017.

Guidotti, C.V., Sassi, F.P., Sassi, R., and Blencoe, J.G., 1994, The effects of ferromagnesian components on the paragonite-muscovite solvus: A semiquantitative analysis based on chemical data for natural paragonite-muscovite pairs: Journal of Metamorphic Geology, v. 12, no. 6, p. 779–788, https://doi.org/10.1111/j.1525-1314.1994.tb00059.x.

Guidotti, C.V., Sassi, F.P., Comodi, P., Zanazzi, P.F., and Blencoe, J.G., 2000, The contrasting responses of muscovite and paragonite to increasing pressure: Petrological implications: The Canadian Mineralogist, v. 38, no. 3, p. 707–712, https://doi.org/10.2113/gscanmin.38.3.707.

Gutiérrez-Alonso, G., et al., 2008a, Rifting along the northern Gondwana margin and the evolution of the Rheic Ocean: A Devonian age for the El Castillo volcanic rocks (Salamanca, Central Iberian Zone): Tectonophysics, v. 461, no. 1–4, p. 157–165, https://doi.org/10.1016/j.tecto.2008.01.013.

Gutiérrez-Alonso, G., Fernández-Suárez, J., Weil, A.B., Murphy, J. Brendan, Nance, R.D., Corfu, F., and Johnston, S.T., 2008b, Self-subduction of the Pangaean global plate: Nature Geoscience, v. 1, p. 549–553, https://doi.org/10.1038/ngeo250.

Halama, R., 2024, Eclogites: Geology Today, v. 40, p. 33–40, https://doi.org/10.1111/gto.12462.

Heinrich, W., and Althaus, E., 1988, Experimental determination of the reactions 4 lawsonite + 1 albite = 1 paragonite + 2 zoisite + 2 quartz + 6 H_2O and 4 lawsonite + 1 jadeite = 1 paragonite + 2 zoisite + 1 quartz + 6 H_2O: Neues Jahrbuch für Mineralogie Monatshefte, v. 11, p. 516–528.

Hemingway, B.S., Bohlen, S.R., Hankins, W.B., Westrum, E.F.J., and Kuskov, O.L., 1998, Heat capacity and thermodynamic properties for coesite and jadeite, reexamination of the quartz-coesite equilibrium boundary: American Mineralogist, v. 83, p. 409–418, https://doi.org/10.2138/am-1998-5-601.

Holland, T., and Blundy, J., 1994, Non-ideal interactions in calcic amphiboles and their bearing on amphibole-plagioclase thermometry: Contributions to Mineralogy and Petrology, v. 116, p. 433–447, https://doi.org/10.1007/BF00310910.

Holland, T., and Powell, R., 2003, Activity-composition relations for phases in petrological calculations; an asymmetric multicomponent formulation: Contributions to Mineralogy and Petrology, v. 145, p. 492–501, https://doi.org/10.1007/s00410-003-0464-z.

Holland, T.J.B., 1979, Experimental determination of the reaction paragonite = jadeite + kyanite + quartz + water, and internally consistent thermodynamic data for part of the system Na_2O-Al_2O_3-SiO_2-H_2O, with applications to eclogites and blueschists: Contributions to Mineralogy and Petrology, v. 68, p. 293–301, https://doi.org/10.1007/BF00371551.

Holland, T.J.B., and Powell, R., 1998, An internally consistent thermodynamic data set for phases of petrological inter-est: Journal of Metamorphic Geology, v. 16, p. 309–343, https://doi.org/10.1111/j.1525-1314.1998.00140.x.

Holland, T.J.B., and Powell, R., 2011, An improved and extended internally consistent thermodynamic dataset for phases of petrological interest, involving a new equation of state for solids: Journal of Metamorphic Geology, v. 29, no. 3, p. 333–383, https://doi.org/10.1111/j.1525-1314.2010.00923.x.

Honarmand, M., Xiao, W., Nabatian, G., Blades, M.L., dos Santos, M.C., Collins, A.S., and Ao, S., 2018, Zircon U-Pb-Hf isotopes, bulk-rock geochemistry and Sr-Nd-Pb isotopes from late Neoproterozoic basement in the Mahneshan area, NW Iran: Implications for Ediacaran active continental margin along the northern Gondwana and constraints on the late Oligocene crustal anatexis: Gondwana Research, v. 57, p. 48–76.

Horton, B.K., Hassanzadeh, J., Stockli, D.F., Axen, G.J., Gillis, R.J., Guest, B., Amini, A., Fakhari, M.D., Zamanzadeh, S.M., and Grove, M., 2008, Detrital zircon provenance of Neoproterozoic to Cenozoic deposits in Iran: Implications for chronostratigraphy and collisional tectonics: Tectonophysics, v. 451, no. 1–4, p. 97–122.

Iizuka, T., and Hirata, T., 2005, Improvements of precision and accuracy in in situ Hf isotope microanalysis of zircon using the laser ablation-MC-ICPMS technique: Chemical Geology, v. 220, no. 1–2, p. 121–137.

Jamei, S., Ghorbani, M., Jafari, A., Williams, I.S., and Moayyed, M., 2021, Geochronology and tectonic significance of A-type granite from Misho, NW Iran: Implications for the detachment of Cimmeria from Gondwana and the opening of Neo-Tethys: Geological Journal, v. 56, p. 5275–5289.

Jenkyns, H.C., 1980. Tethys: Past and present: Proceedings of the Geologists' Association, v. 91, no. 1–2, p. 107–118.

Karimpour, M.H., Stern, C.R., and Farmer, G.L., 2010, Zircon U-Pb geochronology, Sr-Nd isotope analyses, and petrogenetic study of the Dehnow diorite and Kuhsangi granodiorite (Paleo-Tethys), NE Iran: Journal of Asian Earth Sciences, v. 37, p. 384–393.

Kennedy, C.S., and Kennedy, G.C., 1976, The equilibrium boundary between graphite and diamond: Journal of Geophysical Research: Solid Earth and Planets, v. 81, no. 14, p. 2467–2470, https://doi.org/10.1029/JB081i014p02467.

Kirby, G.A., 1979, The Lizard Complex as an ophiolite: Nature, v. 282, 5734, p. 58–61.

Linnemann, U., Pereira, F., Jeffries, T.E., Drost, K., and Gerdes, A., 2008, The Cadomian Orogeny and the opening of the Rheic Ocean: The diacrony of geotectonic processes constrained by LA-ICP-MS U-Pb zircon dating (Ossa-Morena and Saxo-Thuringian Zones, Iberian and Bohemian Massifs): Tectonophysics, v. 461, p. 21–43.

Liou, J.G., Wang, X., Coleman, R.G., Zhang, Z.M., and Maruyama, S., 1989, Blueschists in major suture zones of China: Tectonics, v. 8, no. 3, p. 609–619.

López-Carmona, A., Abati, J., Pitra, P., and Lee, J.K.W., 2014, Retrogressed lawsonite blueschists from the NW Iberian Massif: P–T–t constraints from thermodynamic modelling and $^{40}Ar/^{39}Ar$ geochronology: Contributions to Mineralogy and Petrology, v. 167, https://doi.org/10.1007/s00410-014-0987-5.

Ludwig, K.R., 2009, User's manual for Squid 2.50: A geochronological toolkit for Microsoft Excel: Berkeley Geochronology Center Special Publication, v. 5, p. 110.

Ludwig, K.R., 2012, User's manual for Isoplot 3.75: A geochronological toolkit for Microsoft Excel: Berkeley Geochronology Center Special Publication, v. 5, 75 p.

Mackay-Champion, T.C., Searle, M.P., Tapster, S., Roberts, N.M.W., Shail, R.K., Palin, R.M., Willment, G.H., and Evans, J.T., 2024, Magmatic, metamorphic and structural history of the Variscan Lizard Ophiolite and metamorphic sole, Cornwall, UK: Tectonics, v. 43.

Madanipour, S., Ehlers, T.A., Yassaghi, A., and Enkelmann, E., 2017, Accelerated middle Miocene exhumation of the Talesh Mountains constrained by U-Th/He thermochronometry: Evidence for the Arabia-Eurasia collision in the NW Iranian Plateau: Tectonics, v. 36, p. 1538–1561.

Maruyama, S., Liou, J., and Terabayashi, M., 1996, Blueschists and eclogites of the world and their exhumation: International Geology Review, v. 38, p. 485–594.

Massonne, H.J., and Sobiech, M., 2007, Paragonite: Why is it so rare in medium-temperature high-pressure rocks?: International Geology Review, v. 49, no. 4, p. 301–312.

Mattei, M., Cifelli, F., Alimohammadian, H., Rashid, H., Winkler, A., and Sagnotti, L., 2017, Oroclinal bending in the Alborz Mountains (Northern Iran): New constraints on the age of South Caspian subduction and extrusion tectonics: Gondwana Research, v. 42, p. 13–28.

McKenzie, D., 1972, Active tectonics of the Mediterranean region: Geophysical Journal International, v. 30, no. 2, p. 109–185.

Mirnejad, H., Lalonde, A.E., Obeid, M., and Hassanzadeh, J., 2013, Geochemistry and petrogenesis of Mashhad granitoids: An insight into the geodynamic history of the Paleo-Tethys in northeast of Iran: Lithos, v. 170–171, p. 105–116.

Moazzen, M., Salimi, Z., Rolland, Y., Bröcker, M., and Hajialioghli, R., 2020, Protolith nature and P–T evolution of Variscan metamorphic rocks from the Allahyarlu complex, NW Iran: Geological Magazine, v. 157, no. 11, p. 1853–1876.

Moghadam, H.S., and Stern, R.J., 2014, Ophiolites of Iran: Keys to understanding the tectonic evolution of SW Asia: (I) Paleozoic ophiolites: Journal of Asian Earth Sciences, v. 91, p. 19–38.

Moghadam, H.S., and Stern, R.J., 2015, Ophiolites of Iran: Keys to understanding the tectonic evolution of SW Asia: (II) Mesozoic ophiolites: Journal of Asian Earth Sciences, v. 100, p. 31–59.

Moghadam, H.S., Griffin, W.L., Li, X.-H., Santos, J.F., Karsli, O., Stern, R.J., Ghorbani, G., Gain, S., Murphy, R., and O'Reilly, S.Y., 2017, Crustal evolution of NW Iran: Cadomian Arcs, Archean fragments and the Cenozoic magmatic flare-up: Journal of Petrology, v. 58, p. 2143–2190.

Moores, E.M., 1981, Ancient suture zones within continents: Science, v. 213, 4503, p. 41–46.

Murphy, J.B., and Nance, R.D., 1989, Model for the evolution of the Avalonian-Cadomian belt: Geology, v. 17, p. 735–738.

Murphy, J.B., et al., 2006, Origin of the Rheic Ocean: Rifting along a Neoproterozoic suture?: Geology, v. 34, p. 325–328.

Nance, R.D., Gutiérrez-Alonso, G., Keppie, J.D., Linnemann, U., Murphy, J.B., Quesada, C., Strachan, R.A., and Woodcock, N.H., 2010, Evolution of the Rheic Ocean: Gondwana Research, v. 17, p. 194–222.

Neuerburg, G.J., 1961, A method of mineral separation using hydrofluoric acid: American Mineralogist, v. 46, no. 11–12, p. 1498–1501.

Okamoto, K., and Maruyama, S., 1999, The high pressure stability limits of lawsonite in the MORB + H_2O system: American Mineralogist, v. 84, p. 362–373.

Oliveira, A.L., Schmitz, M.D., Wall, C.J., and Hollanda, M.H.B.M.D., 2022, A bulk annealing and dissolution-based zircon concentration method for mafic rocks: Chemical Geology, v. 597, https://doi.org/10.1016/j.chemgeo.2022.120817.

Omrani, H., Moazzen, M., Oberhänsli, R., Tsujimori, T., Bousquet, R., and Moayyed, M., 2013, Metamorphic history of glaucophane-paragonite-zoisite eclogites from the Shanderman area, northern Iran: Journal of Metamorphic Geology, v. 31, p. 791–812.

Paces, J.B., and Miller, J.D., Jr., 1993, Precise U-Pb ages of Duluth Complex and related mafic intrusions, Northeastern Minnesota: Geochronological insights to physical, petrogenic, paleomagnetic, and tectonomagmatic processes associated with the 1.1 Ga midcontinent rift system: Journal of Geophysical Research: Solid Earth, v. 98, no. B8, p. 13,997–14,013, https://doi.org/10.1029/93JB01159.

Pastor-Galán, D., 2022, From supercontinent to superplate: Late Paleozoic Pangea's inner deformation suggests it was a short-lived superplate: Earth-Science Reviews, v. 226, https://doi.org/10.1016/j.earscirev.2022.103918.

Pastor-Galán, D., Nance, R.D., Murphy, J.B., and Spencer, C.J., 2019, Supercontinents: Myths, mysteries, and milestones: Geological Society, London, Special Publication 470, p. 39–64.

Pastor-Galán, D., Spencer, C.J., Furukawa, T., and Tsujimori, T., 2021, Evidence for crustal removal, tectonic erosion

and flare-ups from the Japanese evolving forearc sediment provenance: Earth and Planetary Science Letters, v. 564, https://doi.org/10.1016/j.epsl.2021.116893.

Patchett, P.J., 1983, Importance of the Lu-Hf isotopic system in studies of planetary chronology and chemical evolution: Geochimica et Cosmochimica Acta, v. 47, p. 81–91.

Paton, C., Hellstrom, J., Paul, B., Woodhead, J., and Hergt, J., 2011, Iolite: Freeware for the visualisation and processing of mass spectrometric data: Journal of Analytical Atomic Spectrometry, v. 26, no. 12, p. 2508–2518.

Pereira, M.F., Chichorro, M., Solá, A.R., Silva, J.B., Sánchez-García, T., and Bellido, F., 2011, Tracing the Cadomian magmatism with detrital/inherited zircon ages by *in-situ* U-Pb SHRIMP geochronology (Ossa-Morena Zone, SW Iberian Massif): Lithos, v. 123, p. 204–217.

Platt, J.P., 1986, Dynamics of orogenic wedges and the uplift of high-pressure metamorphic rocks: Geological Society of America Bulletin, v. 97, p. 1037–1053.

Powell, R., and Holland, T.J.B., 2008, On thermobarometry: Journal of Metamorphic Geology, v. 26, no. 2, p. 155–179.

Rezaeian, M., Kuijper, C.B., van der Boon, A., Pastor-Galán, D., Cotton, L.J., Langereis, C.G., and Krijgsman, W., 2020, Post-Eocene coupled oroclines in the Talesh (NW Iran): Paleomagnetic constraints: Tectonophysics, v. 786.

Rolland, Y., 2017, Caucasus collisional history: Review of data from East Anatolia to West Iran: Gondwana Research, v. 49, p. 130–146.

Rolland, Y., Hässig, M., Bosch, D., Meijers, M.J.M., Sosson, M., Bruguier, O., Adamia, Sh., and Sadradze, N., 2016, A review of the plate convergence history of the East Anatolia-Transcaucasus region during the Variscan: Insights from the Georgian basement and its connection to the Eastern Pontides: Journal of Geodynamics, v. 96, p. 131–145.

Rossetti, F., Monié, P., Nasrabady, M., Theye, T., Lucci, F., and Saadat, M., 2017, Early Carboniferous subduction-zone metamorphism preserved within the Palaeo-Tethyan Rasht ophiolites (western Alborz, Iran): Journal of the Geological Society, v. 174, p. 741–758.

Rotstein, Y., and Kafka, A.L., 1982, Seismotectonics of the southern boundary of Anatolia, eastern Mediterranean region: Subduction, collision, and arc jumping: Journal of Geophysical Research: Solid Earth, v. 87, no. B9, p. 7694–7706, https://doi.org/10.1029/JB087iB09p07694.

Russell, W.A., Papanastassiou, D.A., and Tombrello, T.A., 1978, Ca isotope fractionation on the Earth and other solar system materials: Geochimica et Cosmochimica Acta, v. 42, no. 8, p. 1075–1090, https://doi.org/10.1016/0016-7037(78)90105-9.

Sánchez-García, T., et al., 2014, Early Cambrian granitoids of North Gondwana margin in the transition from a convergent setting to intra-continental rifting (Ossa-Morena Zone, SW Iberia): International Journal of Earth Sciences, v. 103, p. 1203–1218, https://doi.org/10.1007/s00531-013-0939-8.

Sánchez-García, T., Chichorro, M., Solá, A.R., Álvaro, J.J., Díez-Montes, A., Bellido, F., and López-Carmona, A., 2019, The Cambrian-Early Ordovician rift stage in the Gondwanan units of the Iberian Massif, *in* Quesada, C., and Oliveira, J.T., eds., The Geology of Iberia: A Geodynamic Approach: Volume 2: The Variscan Cycle: Cham, Switzerland, Springer Nature, p. 27–74, https://doi.org/10.1007/978-3-030-10519-8_2.

Schaltegger, U., 2007, Hydrothermal zircon: Elements, v. 3, no. 1, p. 51–79, https://doi.org/10.2113/gselements.3.1.51.

Schmidberger, S.S., Simonetti, A., Heaman, L.M., Creaser, R.A., and Whiteford, S., 2007, Lu-Hf, in-situ Sr and Pb isotope and trace element systematics for mantle eclogites from the Diavik diamond mine: Evidence for Paleoproterozoic subduction beneath the Slave craton, Canada: Earth and Planetary Science Letters, v. 254, no. 1–2, p. 55–68, https://doi.org/10.1016/j.epsl.2006.11.020.

Şengör, A.M.C., 1979, Mid-Mesozoic closure of Permo–Triassic Tethys and its implications: Nature, v. 279, no. 5714, p. 590–593, https://doi.org/10.1038/279590a0.

Şengör, A.M.C., 1990, A new model for the late Palaeozoic–Mesozoic tectonic evolution of Iran and implications for Oman, *in* Robertson, A.H.F., Searle, M.P., and Ries, A.C., eds., The Geology and Tectonics of the Oman Region: Geological Society, London, Special Publication 49, p. 797–831, https://doi.org/10.1144/GSL.SP.1992.049.01.49.

Şengör, A.M.C., Yılmaz, Y., and Sungurlu, O., 1984, Tectonics of the Mediterranean Cimmerides: Nature and evolution of the western termination of Palaeo-Tethys, *in* Dixon, J.E., and Robertson, A.H.F., eds., The Geological Evolution of the Eastern Mediterranean: Geological Society, London, Special Publication 17, p. 77–112, https://doi.org/10.1144/GSL.SP.1984.017.01.04.

Şengör, A.M.C., Altner, D., Cin, A., Ustaömer, T., and Hsü, K.J., 1988, Origin and assembly of the Tethyside orogenic collage at the expense of Gondwana Land, *in* Audley-Charles, M.G., and Hallam, A., eds., Gondwana and Tethys: Geological Society, London, Special Publication 37, p. 119–181, https://doi.org/10.1144/GSL.SP.1988.037.01.09.

Shellnutt, J.G., Bhat, G.M., Brookfield, M.E., and Jahn, B.M., 2011, No link between the Panjal Traps (Kashmir) and the Late Permian mass extinctions: Geophysical Research Letters, v. 38, no. 19, https://doi.org/10.1029/2011GL049032.

Shiva, A.N., Yann, R., Magali, R., Delphine, B., Philippe, M., Arthur, L., Olivier, B., and Rahgoshay, M., 2025, Geochronological, isotopic and petrogenetic investigations of Cenozoic Volcanic rocks in the Talysh Massif, NW Iran: Insights for the Eocene magmatic flare-up: Lithos, v. 496–497, https://doi.org/10.1016/j.lithos.2025.107954.

Sláma, J., Košler, J., Condon, D.J., Crowley, J.L., Gerdes, A., Hanchar, J.M., Horstwood, M.S., Morris, G.A., Nasdala, L., Norberg, N., and Schaltegger, U., 2008, Plešovice zircon: A new natural reference material for U-Pb and Hf isotopic microanalysis: Chemical Geology, v. 249, no. 1–2, p. 1–35, https://doi.org/10.1016/j.chemgeo.2007.11.005.

Stacey, J.S., and Kramers, J.D., 1975, Approximation of terrestrial lead isotope evolution by a two- stage model: Earth and Planetary Science Letters, v. 26, p. 207–221.

Stampfli, G.M., Hochard, C., Vérard, C., Wilhem, C., and VonRaumer, J., 2013, The Formation of Pangea: Tectonophysics, v. 593, p. 1–19, https://doi.org/10.1016/j.tecto.2013.02.037.

Tanaka, T., Togashi, S., Kamioka, H., Amakawa, H., Kagami, H., Hamamoto, T., Yuhara, M., Orihashi, Y., Yoneda, S., Shimizu, H., and Kunimaru, T., 2000, JNdi-1: A neodymium isotopic reference in consistency with LaJolla neodymium: Chemical Geology, v. 168, no. 3–4, p. 279–281, https://doi.org/10.1016/S0009-2541(00)00198-4.

Toit, A.L.D., 1937, Our wandering continents: An hypothesis of continental drifting: Oliver and Boyd, 398 p.

Topuz, G., Göçmengil, G., Rolland, Y., Çelik, Ö.F., Zack, T., and Schmitt, A.K., 2013, Jurassic accretionary complex and ophiolite from northeast Turkey: No evidence for the Cimmerian continental ribbon: Geology, v. 41, p. 255–258.

Torsvik, T.H., and Cocks, L.R.M., 2013, Gondwana from top to base in space and time: Gondwana Research, v. 24, 3–4, p. 999–1030.

Tsujimori, T., and Ernst, W.G., 2014, Lawsonite blueschists and lawsonite eclogites as proxies for palaeo-subduction zone processes: A review: Journal of Metamorphic Geology, v. 32, p. 437–454, https://doi.org/10.1111/jmg.12057.

Tsujimori, T., and Mattinson, C., 2021, Eclogites in different tectonic settings, *in* Alderton, D., and Elias, S.A., eds., Encyclopedia of Geology (2nd edition): Amsterdam, Netherlands, Elsevier, p. 561–568, https://doi.org/10.1016/B978-0-08-102908-4.00104-1.

Tsujimori, T., Sisson, V.B., Liou, J.G., Harlow, G.E., and Sorensen, S.S., 2006, Very-low-temperature record of the subduction process: A review of worldwide lawsonite eclogites: Lithos, v. 92, p. 609–624, https://doi.org/10.1016/j.lithos.2006.03.054.

Unterschutz, J.L.E., et al., 2002, North American margin origin of Quesnel terrane strata in the southern Canadian Cordillera: Inferences from geochemical and Nd isotopic characteristics of Triassic metasedimentary rocks: Geological Society of America Bulletin, v. 114, p. 462–475, https://doi.org/10.1130/0016-7606(2002)114<0462:NAMOOQ>2.0.CO;2.

van der Boon, A., van Hinsbergen, D.J.J., Rezaeian, M., Gürer, D., Honarmand, M., Pastor-Galán, D., Krijgsman, W., and Langereis, C.G.G., 2018, Quantifying Arabia–Eurasia convergence accommodated in the Greater Caucasus by paleomagnetic reconstruction: Earth and Planetary Science Letters, v. 482, https://doi.org/10.1016/j.epsl.2017.11.025.

Van der Voo, R., 1993, Paleomagnetism of the Atlantic, Tethys and Iapetus Oceans: Cambridge, UK, Cambridge University Press, 411 p., https://doi.org/10.1017/CBO9780511524936.

Van der Voo, R., and French, R.B., 1974, Apparent polar wandering for the Atlantic-bordering continents: Late Carboniferous to Eocene: Earth-Science Reviews, v. 10, 2, p. 99–119, https://doi.org/10.1016/0012-8252(74)90082-8.

van Hinsbergen, D.J.J., Torsvik, T.H., Schmid, S.M., Maţenco, L.C., Maffione, M., Vissers, R.L.M., Gürer, D., and Spakman, W., 2020, Orogenic architecture of the Mediterranean region and kinematic reconstruction of its tectonic evolution since the Triassic: Gondwana Research, v. 81, p. 79–229, https://doi.org/10.1016/j.gr.2019.07.009.

Vasey, D.A., Cowgill, E., Roeske, S.M., Niemi, N.A., Godoladze, T., Skhirtladze, I., and Gogoladze, S., 2020, Evolution of the Greater Caucasus basement and formation of the Main Caucasus Thrust, Georgia: Tectonics, v. 39, 3, https://doi.org/10.1029/2019TC005828.

Vermeesch, P., 2018, IsoplotR: A free and open toolbox for geochronology: Geoscience Frontiers, v. 9, p. 1479–1493, https://doi.org/10.1016/j.gsf.2018.04.001.

Vervoort, J.D., Patchett, P.J., Söderlund, U., and Baker, M., 2004, Isotopic composition of Yb and the determination of Lu concentrations and Lu/Hf ratios by isotope dilution using MC-ICPMS: Geochemistry, Geophysics, Geosystems, v. 5, https://doi.org/10.1029/2004GC000721.

Vielzeuf, D., and Schmidt, M.W., 2001, Melting relations in hydrous systems revisited: Application to metapelites, metagraywackes and metabasalts: Contributions to Mineralogy and Petrology, v. 141, p. 251–267, https://doi.org/10.1007/s004100100237.

Wan, B., Chu, Y., Chen, L., Liang, X., Zhang, Z., Ao, S., and Talebian, M., 2021, Paleo-Tethys subduction induced slab-drag opening the Neo-Tethys: Evidence from an Iranian segment of Gondwana: Earth-Science Reviews, v. 221, https://doi.org/10.1016/j.earscirev.2021.103788.

Warr, L.N., 2021, IMA-CNMNC approved mineral symbols: Mineralogical Magazine, v. 85, 3, p. 291–320, https://doi.org/10.1180/mgm.2021.43.

Wasserburg, G.J., Jacobsen, S.B., DePaolo, D.J., McCulloch, M.T., and Wen, T., 1981, Precise determination of Sm Nd ratios, Sm and Nd isotopic abundances in standard solutions: Geochimica et Cosmochimica Acta, v. 45, 12, p. 2311–2323, https://doi.org/10.1016/0016-7037(81)90088-5.

Wegener, A., 1912, Die entstehung der kontinente: Geologische Rundschau, v. 3, 4, p. 276–292, https://doi.org/10.1007/BF02202896.

Weil, A.B., Gutiérrez-Alonso, G., Johnston, S.T., and Pastor-Galán, D., 2013, Kinematic constraints on buckling a lithospheric-scale orocline along the northern margin of Gondwana: A geologic synthesis: Tectonophysics, v. 582, p. 25–49, https://doi.org/10.1016/j.tecto.2012.10.006.

White, R.W., Powell, R., Holland, T.J.B., and Worley, B.A., 2000, The effect of TiO_2 and Fe_2O_3 on metapelitic assemblages at greenschist and amphibolite facies conditions: Mineral equilibria calculations in the system K_2O-FeO-MgO-Al_2O_3-SiO_2-H_2O-TiO_2-Fe_2O_3: Journal of Metamorphic Geology, v. 18, p. 497–511, https://doi.org/10.1046/j.1525-1314.2000.00269.x.

White, R.W., Powell, R., and Johnson, T.E., 2014, The effect of Mn on mineral stability in metapelites revisited: New a-x relations for manganese-bearing minerals: Journal of Metamorphic Geology, v. 32, p. 809–828, https://doi.org/10.1111/jmg.12095.

Williams, I.S., 1998, U-Th-Pb geochronology by ion microprobe, *in* McKibben, M.A., Shanks III, W.C., and

Ridley, W.L., eds., Applications of microanalytical techniques to understanding mineralizing processes: Reviews in Economic Geology, v. 7, p. 1–35.

Wu, L., Murphy, J.B., Quesada, C., Li, Z.-X., Waldron, J.W.F., Williams, S., Pisarevsky, S., and Collins, W.J., 2021, The amalgamation of Pangea: Paleomagnetic and geological observations revisited: Geological Society of America Bulletin, v. 133, p. 625–646, https://doi.org/10.1130/B35633.1.

Zanchetta, S., Zanchi, A., Villa, I., Poli, S., and Muttoni, G., 2009, The Shanderman eclogites: A Late Carboniferous high-pressure event in the NW Talesh Mountains (NW Iran), *in* Brunet, M.F., Wilmsen, M., and Granath, J.W., eds., South Caspian to Central Iran Basins: Geological Society, London, Special Publication 312, p. 57–78, https://doi.org/10.1144/SP312.4.

Zanchi, A., Zanchetta, S., Berra, F., Mattei, M., Garzanti, E., Molyneux, S., Nawab, A., and Sabouri, J., 2009a, The Eo-Cimmerian (Late? Triassic) orogeny in North Iran, *in* Brunet, M.F., Wilmsen, M., and Granath, J.W., eds., South Caspian to Central Iran Basins: Geological Society, London, Special Publication 312, p. 31–55, https://doi.org/10.1144/SP312.3.

Zanchi, A., Zanchetta, S., Garzanti, E., Balini, M., Berra, F., Mattei, M., and Muttoni, G., 2009b, The Cimmerian evolution of the Nakhlak-Anarak area, Central Iran, and its bearing for the reconstruction of the history of the Eurasian margin, *in* Brunet, M.F., Wilmsen, M., and Granath, J.W., eds., South Caspian to Central Iran Basins: Geological Society, London, Special Publication 312, p. 261–286, https://doi.org/10.1144/SP312.13.